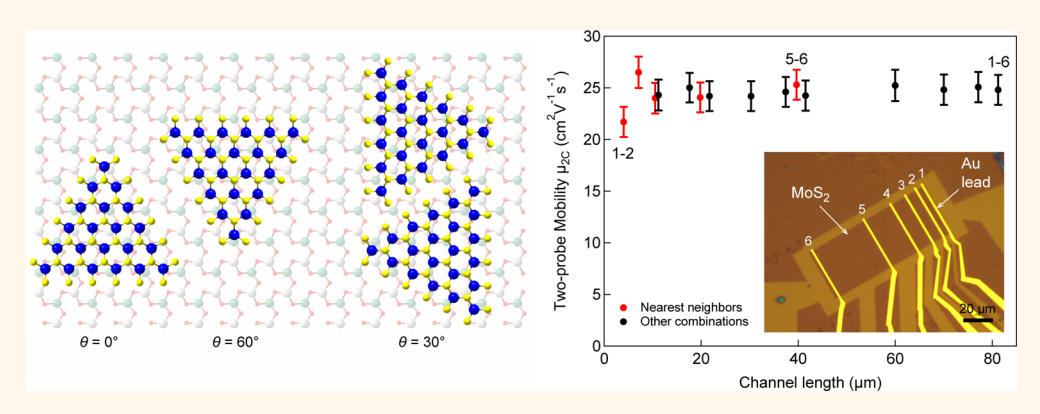


Large-Area Epitaxial Monolayer MoS₂

Dumitru Dumcenco,^{†,#} Dmitry Ovchinnikov,^{†,#} Kolyo Marinov,^{†,#} Predrag Lazić,[‡] Marco Gibertini,[§] Nicola Marzari,[§] Oriol Lopez Sanchez,[†] Yen-Cheng Kung,[†] Daria Krasnozhon,[†] Ming-Wei Chen,[†] Simone Bertolazzi,[†] Philippe Gillet,^{||} Anna Fontcuberta i Morral,[§] Aleksandra Radenovic,[⊥] and Andras Kis^{*,†}

†Electrical Engineering Institute, ^{\$I}Institute of Materials, ^{II}Institute of Condensed Matter Physics, and ^LInstitute of Bioengineering, Ecole Polytechnique Federale de Lausanne (EPFL), CH-1015 Lausanne, Switzerland and [‡]Institute Ructer Bošković (IRB), HR-10000 Zagreb, Croatia. [#]D. Dumcenco, D. Ovchinnikov, and K. Marinov contributed equally.

ABSTRACT



Two-dimensional semiconductors such as MoS_2 are an emerging material family with wide-ranging potential applications in electronics, optoelectronics, and energy harvesting. Large-area growth methods are needed to open the way to applications. Control over lattice orientation during growth remains a challenge. This is needed to minimize or even avoid the formation of grain boundaries, detrimental to electrical, optical, and mechanical properties of MoS_2 and other 2D semiconductors. Here, we report on the growth of high-quality monolayer MoS_2 with control over lattice orientation. We show that the monolayer film is composed of coalescing single islands with limited numbers of lattice orientation due to an epitaxial growth mechanism. Optical absorbance spectra acquired over large areas show significant absorbance in the high-energy part of the spectrum, indicating that MoS_2 could also be interesting for harvesting this region of the solar spectrum and fabrication of UV-sensitive photodetectors. Even though the interaction between the growth substrate and MoS_2 is strong enough to induce lattice alignment *via* van der Waals interaction, we can easily transfer the grown material and fabricate devices. Local potential mapping along channels in field-effect transistors shows that the single-crystal MoS_2 grains in our film are well connected, with interfaces that do not degrade the electrical conductivity. This is also confirmed by the relatively large and length-independent mobility in devices with a channel length reaching 80 μ m.

KEYWORDS: two-dimensional materials \cdot MoS₂ \cdot epitaxial growth \cdot electronic transport \cdot grain boundaries \cdot Kelvin probe force microscopy

he most investigated member of the transition metal dichalcogenide (TMD) family, molybdenum disulfide (MoS₂), has attracted widespread attention for a variety of next-generation electrical and optoelectronic device applications because of its unique properties. In the bulk, this material has a crystalline structure consisting of covalently bonded layers weakly coupled to each other by weak van der Waals (vdW) forces. Owing to the weak coupling, two-dimensional (2D) monolayer MoS₂ can be easily obtained by exfoliation using Scotch tape¹ or liquid-phase

exfoliation.^{2,3} Whereas bulk MoS₂ is a semiconductor with an indirect band gap of 1.2 eV,⁴ monolayer MoS₂ is a direct gap semiconductor with a band gap of at least 1.8 eV⁵⁻⁸ due to the 2D confinement.⁸ It also has Raman-active modes that are very sensitive to the thickness, which provides a convenient method for determining the number of layers with a reliable precision⁹ in addition to atomic force microscopy and optical detection techniques.¹⁰ The dramatic difference in the electronic structure of monolayer MoS₂ in comparison with its bulk counterpart offers many opportunities

* Address correspondence to andras.kis@epfl.ch.

Received for review February 27, 2015 and accepted March 30, 2015.

Published online 10.1021/acsnano.5b01281

© XXXX American Chemical Society

for diverse applications. Using 2D crystals of MoS₂ mechanically exfoliated from bulk geological samples, versatile devices including field-effect transistors with high on/off current ratio,¹⁰ memory cells,¹¹ ultrasensitive photodetectors,^{12,13} and nanopores¹⁴ have been reported. Because MoS₂ has a high mechanical flexibility and breaking strength,¹⁵ all these devices can in principle be implemented on flexible substrates.¹⁶

However, exfoliation of geological material and samples grown using chemical vapor transport¹⁷ lacks the systematic control of the thickness, size, and uniformity of the 2D film and is not scalable for large-scale device fabrication. Because of this, several methods, such as decomposition of thiomolybdates 18 and sulfurization of Mo metal¹⁹ or molybdenum oxide, 20-22 have been exploited to synthesize MoS₂ on diverse substrates. Among them, chemical vapor deposition (CVD) is the most promising method to synthesize monolayer MoS2 triangular islands tens of micrometers in size.²⁰⁻²² In most of these reports, SiO₂ was used as the growth substrate, resulting in the random orientation of MoS₂ domains because of the amorphous nature of the substrate and its relatively high surface roughness. This inevitably results in a large concentration of grain boundaries that can be detrimental to the electrical^{23,24} and mechanical properties of the grown films over length scales exceeding several micrometers. In order to avoid this, it is necessary to control the crystallographic orientation of MoS₂ islands during growth so that they can coalesce into a uniform layer with a reduced density of grain boundaries.

Such control could in practice be achieved using a suitable atomically smooth crystalline substrate. In the case of classical three-dimensional materials this is normally achieved using epitaxial growth. Recently, van der Waals epitaxy has shown its potential for circumventing the need for a lattice-matched substrate and still keeping an ordered relation with the substrate. 25,26 Van der Waals interaction between the substrate surface and the grown material governs the formation of the initial nuclei (islands), which constitute the precursors of the layers. Only energetically stable nuclei are able to grow by lateral spreading through the lateral facets. This leads to an overall preferential orientation of the grown layers. The relatively low strength of the van der Waals interaction and the relaxed requirement for lattice matching for substrates and overlayers without dangling bonds make it difficult in practice to control the lattice orientation of the deposited films. This was the case in previously reported deposition of centimeter-scale monolayer MoS₂ films that have been deposited on other layered materials such as mica 27 or graphene, $^{28-30}$ where MoS₂ grains showed a wide distribution of orientations with respect to each other and the substrate lattice.

RESULTS AND DISCUSSION

Here, we use highly polished, EPI-ready grade sapphire substrates to achieve control over lattice orientation during CVD growth of monolayer MoS2. Such crystals are commonly used as growth substrates for GaN growth in LED manufacturing and for the growth of III-V high electron mobility transistors.31 Even though MoS₂ and sapphire interact only via the relatively weak van der Waals interaction, commensurability of the sapphire lattice with MoS₂ allows the van der Waals interaction to control the lattice orientation of MoS₂ in a similar way to the lattice matching requirement in covalent semiconducting materials. While growth of MoS₂³² and TMDs³³ on sapphire substrates has been reported before, this is the first time control over lattice orientation with centimeter-scale uniformity has been achieved during the growth of a monolayer 2D semiconductor, and it opens the way to largearea growth of high-quality MoS₂. Key to achieving such lattice orientation is in the preparation of atomically smooth sapphire terraces on the surface of sapphire by annealing it in air for 1 h at a temperature of 1000 °C just prior to the growth process (Supporting Figure S1).34 An AFM-based analysis shows that the sapphire surface is characterized by atomically flat terraces \sim 50-70 nm wide with a step height of 0.22 nm due to a small miscut angle estimated to be \sim 0.2°. The terrace edges follow the [11 $\overline{2}$ 0] direction on average.³⁵ Annealed samples are transferred to the CVD system, and growth occurs. The growth process is based on the gas-phase reaction between MoO₃ and sulfur evaporated from solid sources^{21,22} using ultrahigh-purity argon as the carrier gas.

The growth procedure results in characteristic single-crystal domains in the shape of well-defined equilateral triangles that merge into a continuous monolayer film covering a typical area of 6 mm \times 1 cm in the middle portion of the growth substrate, Figure 1a. Figure 1b presents optical images of regions showing partial (top image) and almost full (bottom) coverage. A careful examination of a region with incomplete coverage, Figure 1c, reveals that most of the single-crystal domain edges are oriented along dominant directions. A reflection high-energy electron diffraction (RHEED) pattern is shown in the inset of Figure 1c. The appearance of streaks typical of 2D materials and the MoS_2 (1×1) pattern indicate the growth of a homogeneous and well-structured film over a large area. The majority (91.5% of islands shown in Figure 1c) of single-crystal domains are well aligned with the relative orientation of edges that can be expressed as multiples of 60°. This is confirmed by the orientation histogram presented in Figure 1f for the same area as in Figure 1c, showing that the dominant edge orientations are 0° and $\pm 60^{\circ}$. A small fraction of domains (6% of islands in Figure 1c) show edges with a

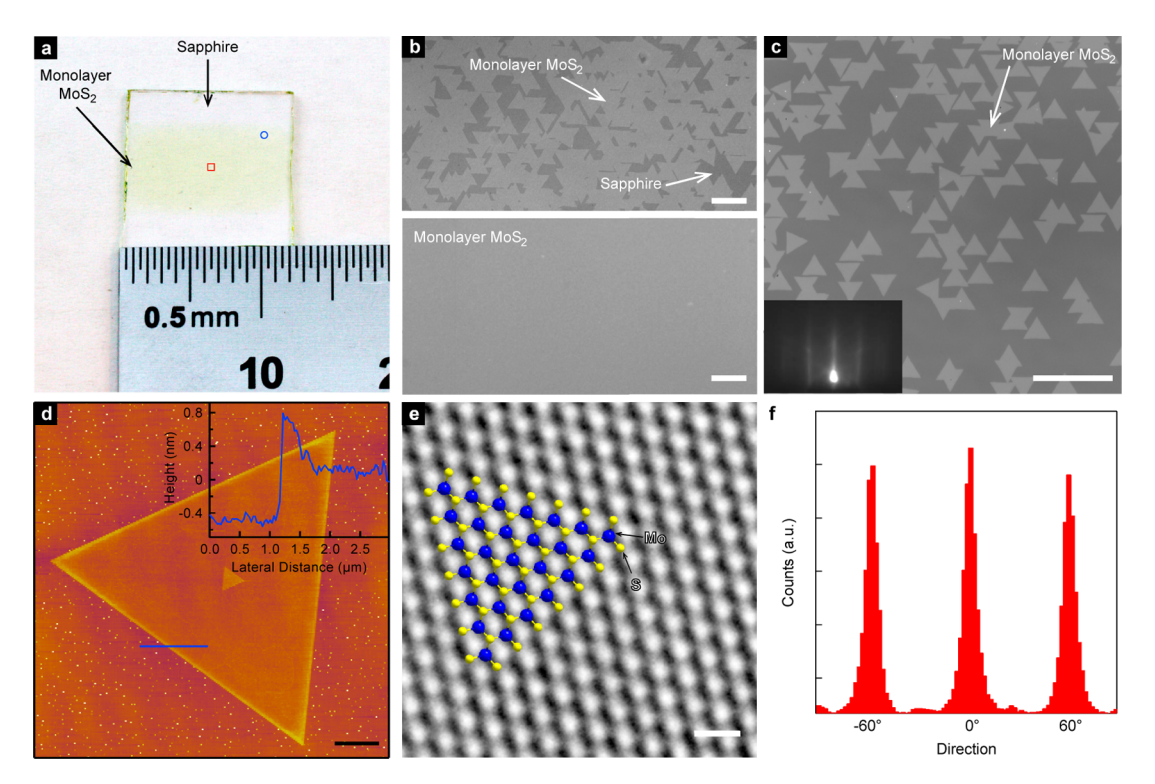


Figure 1. Monolayer MoS_2 growth with controlled lattice orientation. (a) Photograph of centimeter-scale monolayer MoS_2 grown on sapphire. (b) Optical microscopy images from different regions of the sample showing incomplete coverage close to the edges (upper image, position marked by the circle in a) and full coverage close to the center of the growth substrate (lower image, position marked by the rectangle in a). Scale bar length is $20~\mu m$ on the top image and $10~\mu m$ for the bottom image. Original optical images were converted to grayscale, and the contrast was enhanced. (c) Optical microscopy image of monolayer MoS_2 grains grown on atomically smooth sapphire. Scale bar length is $50~\mu m$. Inset: RHEED pattern acquired on the CVD-grown sample showing a film with long-range structural order. (d) Atomic force microscope image of a monolayer MoS_2 grain. Scale bar is $2~\mu m$ long. Inset: Line scan showing the thickness profile along the blue line in the AFM image. (e) High-resolution TEM image of a suspended MoS_2 film showing the crystallinity of the sample. View of the structural model is overlaid. Scale bar is 0.5~n m long. (f) Orientation histogram based on the area shown in part c confirms that the majority of MoS_2 grain edges are oriented along 0° and $\pm 60^\circ$ angles.

relative angle of $\pm 30^{\circ}$, while the rest (2.5%) show other orientations.

Figure 1d shows an AFM image of a single crystal of monolayer MoS₂. According to previous STM studies, these MoS₂ edges are expected to be $(10\overline{10})$ Mo zigzag edges likely terminated with sulfur.³⁶ The sapphire terrace step height of 0.22 nm is sufficiently low to ensure the growth of continuous MoS₂ single crystals, as confirmed by TEM imaging and electrical transport measurements. Figure 1e shows a high-resolution TEM image of a freestanding membrane³⁷ of monolayer MoS₂ showing its regular atomic structure with a clearly discernible hexagonal symmetry. White spots correspond to holes in the atomic structure, while dark spots correspond to sulfur and molybdenum atoms.

We first check the quality of our large-area monolayer MoS_2 films by performing optical characterization. Figure 2a shows typical Raman spectra of the CVD material compared to monolayer MoS_2 exfoliated onto sapphire. The spectra show two characteristic peaks in this spectral range: the out-of-plane vibration of S atoms (A'_1) with a Raman shift of \sim 405 cm $^{-1}$ and the in-plane vibration of Mo and S atoms (E') at

 \sim 385 cm $^{-1.9}$ The observed frequency difference confirms that the deposited material is monolayer MoS₂. The ratio between the A $_1$ and E' mode intensities can be used as an indicator of doping levels,³⁸ and it indicates that the CVD material is less doped than the exfoliated counterpart. Another indication of a smaller structural disorder³⁹ in the CVD material is the smaller width of the A $_1$ mode.

Figure 2b shows a photoluminescence spectrum acquired at room temperature on CVD-grown and adhesive tape exfoliated monolayer MoS2. We can clearly resolve the intense A excitonic peak at 659 nm (1.88 eV), while the B exciton is not expected to be visible at low excitation intensities due to statefilling effects.40 Typical peak widths are ~26 nm (\sim 72 meV) and are smaller than in exfoliated MoS₂ samples (\sim 40 nm or \sim 111 eV), indicating that our CVD MoS₂ has superior optical qualities to the exfoliated material. Relative photoluminescence (PL) intensities also indicate a reduced doping level in the CVD material. Detailed photoluminescence mapping of single domains did not resolve any internal structure, indicating the absence of internal grain boundaries.

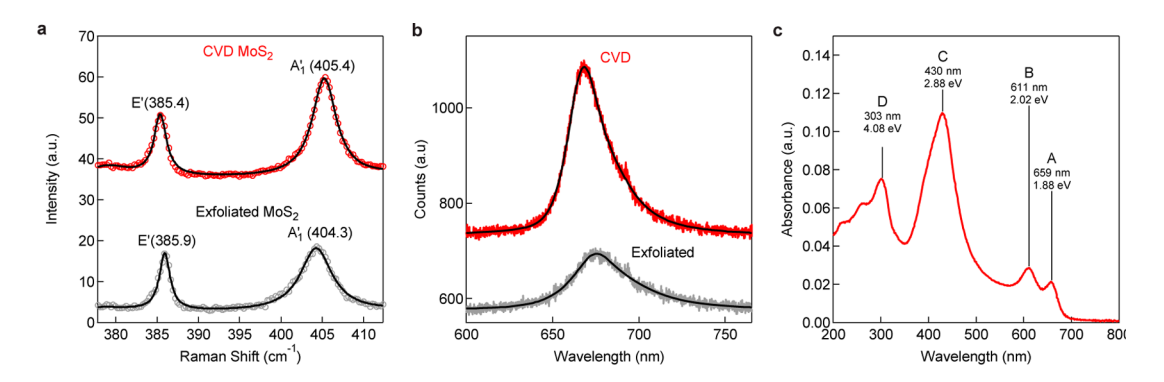


Figure 2. Optical properties of large-area monolayer MoS₂. (a) Raman spectra of as-grown monolayer MoS₂ on sapphire and monolayer MoS₂ exfoliated from bulk crystals and transferred onto sapphire. (b) Photoluminescence spectra of as-grown monolayer MoS₂ on sapphire and monolayer MoS₂ exfoliated from bulk crystals onto sapphire. Black lines in parts a and b correspond to fits. (c) UV—vis optical absorbance spectra acquired from large-area monolayer MoS₂ showing the A and B absorption peaks due to band-edge excitons as well as C and D peaks associated with van Hove singularities of MoS₂.

Thanks to the optical transparency of the sapphire substrate and the large area of the sample covered by monolayer MoS₂, we can perform UV-visible absorption characterization using a simple benchtop spectrophotometer. The resulting spectrum shown in Figure 2c represents broadband absorbance measurements on MoS₂. The spectrum shows the well-known A and B excitonic absorption bands at 695 nm (1.78 eV) and 611 nm (2.02 eV).^{6,7} This demonstrates the high optical quality and uniformity of our monolayer MoS₂ over a large area. In addition, we can also clearly observe the recently reported C peak at 430 nm (2.88 eV)⁴¹ as well as the D peak at 303 nm (4.08 eV). Whereas the A and B peaks are associated with optical absorption by band-edge excitons, peaks C and D are associated with van Hove singularities⁴² of monolayer MoS₂. The fact that MoS₂ shows enhanced absorbance in the 200-500 nm range along with the relatively high mobility of the material could play an important role in designing solar cells and UVsensitive photodetectors.

We proceed to analyze the large-scale crystal structure and its relative orientation using bright-field TEM imaging and selected-area electron diffraction. The asymmetry of the Mo and S sublattices allows us to determine the orientation of the MoS₂ lattice with respect to the island edges (Supporting Section 3)^{22,37} and to confirm that the observed single-crystal domains share the same lattice orientation within the grains. This allows us to identify the lattice orientation based on the orientation of the triangular single crystals.

Figure 3a shows a low-magnification image of the group of aligned MoS₂ triangular islands. We closely examine a small region involving two neighboring islands by positioning the select-area aperture at the red circle containing two islands with their edges forming a 60° angle and acquiring the diffraction pattern shown in the inset of Figure 3a. Even though this diffraction pattern has been acquired from both triangles, we can observe only one set of diffraction

spots with 6-fold symmetry, showing the precise alignment of lattices in both of the islands. Figure 3b shows another example of a much less frequently occurring situation with two islands merging under a 90° angle. In this case, we can clearly distinguish two sets of $[\overline{1}100]$ diffraction spots, rotated by 30° .

Figure 3c schematically illustrates the most likely relative orientations for monolayer MoS_2 growing epitaxially on the atomically smooth surface of sapphire, corresponding to $\sim 97\%$ of the observed grain orientations. The 0° and 60° orientations correspond to the 3-on-2 superstructure of MoS_2 (lattice constant 3.212 Å) and sapphire (lattice constant 4.814 Å).

In order to explain the presence of privileged growth orientations for MoS₂ islands on sapphire, we have first performed first-principles, van der Waals corrected density functional theory (DFT) simulations of MoS₂covered sapphire. These calculations confirm that the interactions between MoS₂ and the sapphire surface are of vdW nature and magnitude (see Supporting Section 4). DFT calculations need to be performed in the coincident-site lattice of common supercells in which the MoS₂ monolayers are in registry with the substrate. Since these cells exhibit a limited size, some amount of artificial strain needs to be introduced in order to limit the size of the supercells used. In reality, the MoS₂ overlayers are not expected to show much strain²⁶ because of their weak vdW interactions with the substrate. The strain energy turns out to be of similar magnitude to the vdW interaction energy with the substrate. As a consequence, it becomes difficult to ascertain the stability of one orientation with respect to another from DFT calculations alone. On the other hand, these results also clearly point to a vdW nature for the interactions. This prompted us to construct a simple model of adsorption accounting only for pairwise atom-atom interactions of a $-C_6/r_6$ nature. To our surprise, this model shows an extremely rich adsorption phenomenology that is in agreement with the experimental findings, notably, pointing out that

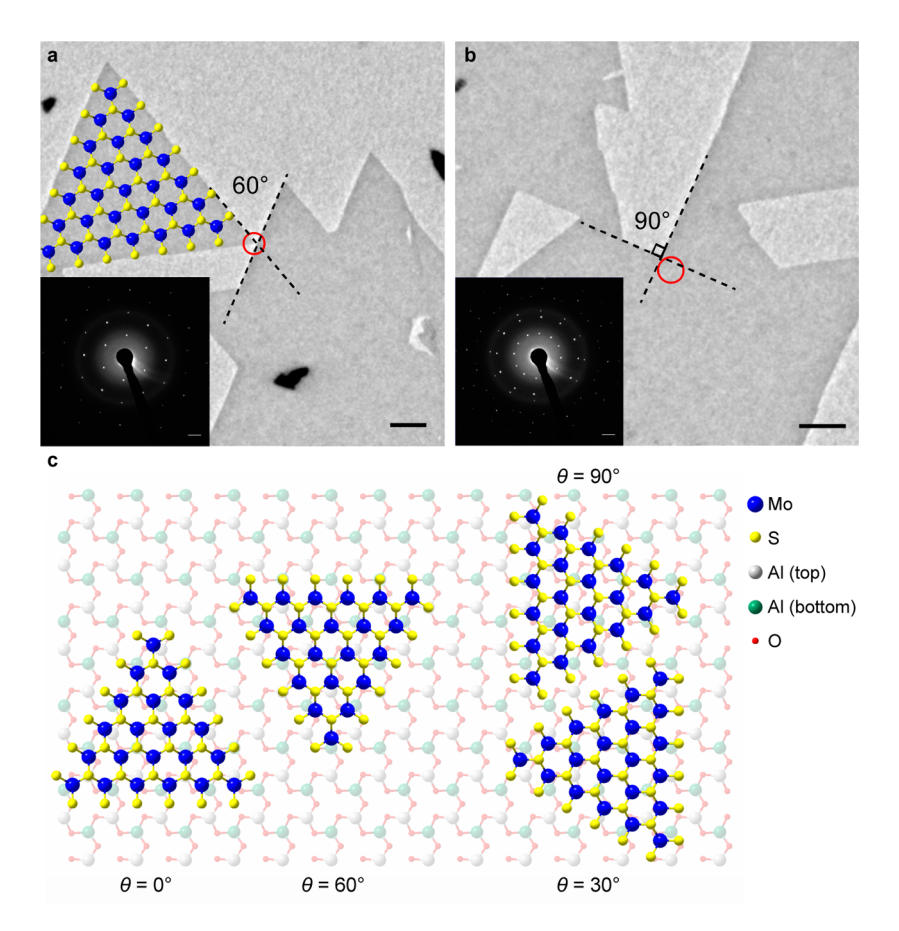


Figure 3. Diffraction patterns from different island orientations. (a) Low-magnification TEM image of several neighboring MoS_2 islands. The diffraction pattern acquired from the area denoted with the red circle is shown in the inset and corresponds to the most common arrangement between neighboring islands. Only one set of diffraction spots can be detected from such islands, indicating that their crystalline lattices are aligned. The MoS_2 structure drawing indicates the lattice orientation within the single-crystal island and is not to scale. (b) Low-magnification TEM image and the corresponding diffraction patterns from two merging islands with their edges forming a 90° angle. Two sets of diffraction spots, rotated by 30°, can be observed, indicating a 30° lattice misorientation angle. (c) Schematic drawing showing the top view of relative lattice orientations between monolayer MoS_2 and c-plane sapphire. In the case of the arrangement of the left-hand side, corresponding to lattice rotation angles $\theta = 0^\circ$ and $\theta = 60^\circ$, the two lattices are commensurate. Two minority orientations can be observed in our sample, corresponding to a lattice rotation angle $\theta = 30^\circ$ and $\theta = 90^\circ$ (right-hand side).

only MoS₂ configurations at either 0° or 60° equivalent orientations (see Figure 3c) provide a structured potential energy surface that is sensitive to arbitrary in-plane translations of the MoS₂ plane, and with welldefined maxima and minima in the adsorption energies (Figure 4). All other orientations yield instead a flat energy surface where the adsorption energy is completely independent of translations and rotations of MoS₂ with respect to the surface. From this, we can conclude that the MoS₂ layer would be free to rotate and slide along the surface of sapphire until it would find the orientation and positions of strongest adsorption. The oriented growth of MoS₂ would proceed as follows: using low supersaturation conditions very few MoS₂ nuclei are formed and grow laterally on the substrate. Weak (vdW) interactions with the substrate guarantee a certain degree of rotation/translation with respect to the surface in the initial phase. When the nucleus reaches a certain size, not only is it stable against decomposition but it gets pinned down in the

most stable orientation with the substrate. Growth proceeds then forming a continuous and oriented layer. We cannot help but see the analogy of this pinning process with the process of attaching a Lego brick onto another larger Lego brick surface, in an analogy introduced by A. Geim in ref 43. Last, the presence of surface defects could be at the origin of less frequently observed lattice orientations.

We characterize the electrical quality of constituent grains by performing electrical transport measurements on single grains (Supporting Section 5). Results show that the mobility reaches a value of 43 cm²/(V s), comparable to results from previous two-terminal measurements on CVD MoS₂ (ref 44) and slightly higher than in devices based on exfoliated MoS₂ prepared in the same way.^{45,46} Good stitching of such high-quality single crystals into continuous films is necessary in order to realize large-area MoS₂ with the same quality as that of the single crystal. We first study the influence of grain boundaries on the electrical

properties of MoS₂, by measuring local electrical potentials using scanning Kelvin probe microscopy⁴⁷ (SKPM), on back-gated MoS₂ field-effect transistors (FETs) incorporating two grains possibly separated by a grain boundary. The advantage of this method over conventional techniques such as FET device characterization using the transfer length method is that it allows direct imaging of the impact of nanoscale features such as grain boundaries in laterally inhomogeneous materials. With this AFM-based method, we can record

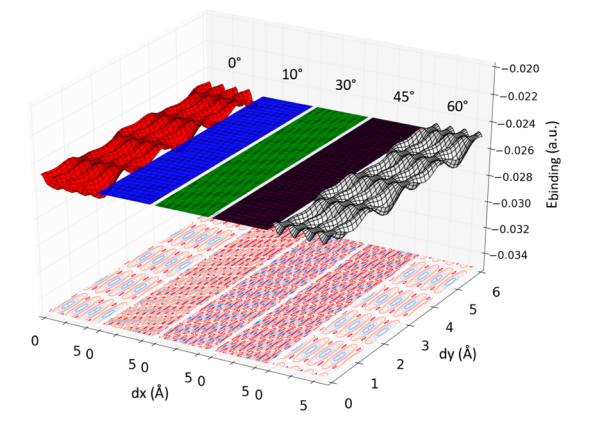


Figure 4. Binding energies for MoS₂ and sapphire. Data are shown as a 3D surface and contour plot of relative binding energies for MoS₂ on sapphire, for different relative lattice orientations and as a function of relative shift in x- and y-directions, corresponding to the lateral motion of the MoS₂ monolayer on the surface of atomically smooth sapphire. Only the 0° and 60° orientations result in significant corrugation and substantial stable minima. The distance between MoS₂ and sapphire is 3.24 Å, as obtained from DFT calculations.

the local variation of the local potential of the surface, relative to the metallic probe. Grain boundaries that contribute additional electrical resistance and degrade device mobility readily show up on such scans (Supporting Section 6). Figure 5 shows local potential maps (upper panels) and potential line scans (lower panels) across the three types of conjoined single-crystal MoS₂ grains that account for pairs formed by orientations shown in Figure 3c. All other possible combinations involving pairs composed of any of the MoS₂ lattice and triangle orientations shown in Figure 3c can be reduced to these three misorientation angles. Figure 5a shows measurements acquired across two grains sharing the same crystalline orientation. In this case, the two grains can join without the appearance of a grain boundary, while in the case of merged single crystals shown in Figure 5b and c with relative lattice orientations characterized by the misorientation angles $\theta_{\rm rel}$ = 60° and $\theta_{\rm rel}$ = 30°, a grain boundary is expected to be present at their interface. Potential line scans, acquired along the red lines overlaid on the potential maps for all three configurations, show a clear monotonic drop of the voltage between the contacts, revealing the absence of an additional voltage drop (resistance) due to the presence of a grain boundary. This shows that for misorientation angles $\theta_{\rm rel} = 60^{\circ}$ and $\theta_{\rm rel} = 30^{\circ}$ occurring in our samples, the single crystals are joined by twin grain boundaries, previously shown not to degrade the electrical properties of polycrystalline MoS₂. ^{22,23} This proves that the epitaxial growth of MoS₂ on sapphire, providing these predominant domain

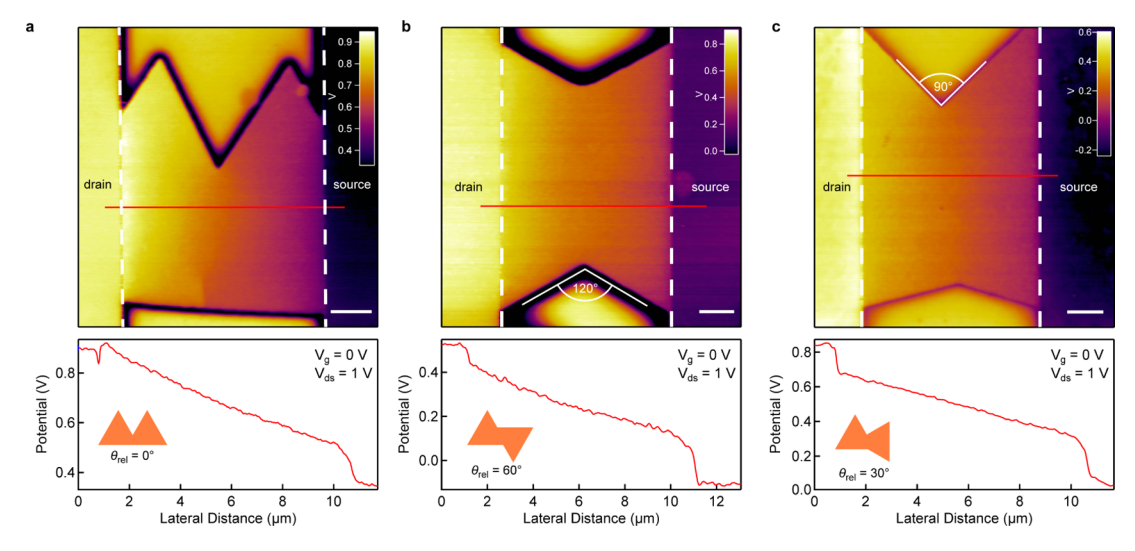


Figure 5. Mapping the local electrical properties across grain boundaries in large-area monolayer MoS₂. (a) Local potential map (upper panel) and line scan across the red line (lower panel) showing the potential drop over the conductive channel of a biased field-effect transistor based on two merged MoS2 single crystals with the same lattice orientation. In this case, no grain boundary is expected. The smooth potential drop indicates the absence of abrupt changes of potential that would indicate the presence of an electrically resistive grain boundary. (b) Local potential map and line scan over two merged triangles with a 60° misorientation angle. This configuration is expected to result in a twin grain boundary. Its presence does not introduce an extra potential drop, indicating that it does not degrade the electrical conductivity of the material. (c) Local potential map and line scan over two merged triangles with a 30° misorientation angle. The presence of the grain boundary does not introduce an extra potential drop in the channel. Insets in line scan plots indicate relative orientations of MoS₂ single crystals. Scale bars are 2 μ m long.

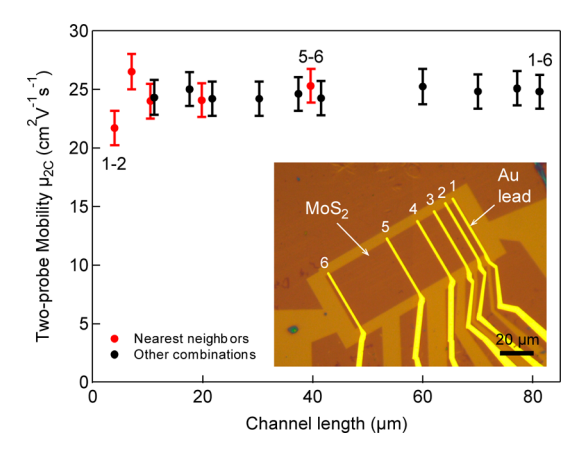


Figure 6. Electrical properties of large-area devices. Field-effect mobility as a function of channel length. Values are extracted from two-contact measurements performed on the device based on the continuous film shown in the inset with Au leads labeled 1–6. Red symbols correspond to values obtained using two nearest neighbor electrodes as source and drain terminals with the longest segment between electrodes 5 and 6 having a length of 39.7 μ m. Black symbols denote values extracted by using other combinations of electrodes with the longest segment between terminals 1 and 6 having a length of 81.2 μ m.

orientations, can dramatically suppress the formation of tilted grain boundaries, which are detrimental for the electrical properties of the polycrystalline material, and that epitaxial growth of MoS₂ is crucial for the formation of nonresistive grain boundaries in a polycrystalline film. We now turn to polycrystalline films and examine their electrical properties by performing measurements on a section of a continuous film with a length $L=81.2~\mu m$ and width $W=36.6~\mu m$, contacted by multiple electrodes (Supporting Section 7). The effective field-effect mobility as a function of channel length, extracted from two contact measurements in various lead configurations, is shown in Figure 6. We observe no degradation in mobility with increasing length from 4 μ m to \sim 80 μ m, within the measurement error. We compare our findings with recent results²³ on polycrystalline continuous CVD MoS₂ films, where the material was grown on SiO₂ with random relative orientation of grains as well as bilayer formation on grain boundaries influencing electrical transport properties. In our case these sources of scattering are eliminated and mobility stays constant in the devices built on multiple merged grains. We estimate that there are \sim 16 junctions between single crystals along the length of the 82 μ m channel (Supporting Section 7). This shows that the superior electrical properties of the single crystals are preserved over length scales larger than those corresponding to single grains.

CONCLUSIONS

In conclusion, we have achieved epitaxial chemical vapor deposition growth of monolayer MoS₂ with a high degree of control over lattice orientation by using atomically smooth surfaces of sapphire as the growth substrate. The large-area MoS₂ film is formed from merging single-crystalline domains, with the majority of the domains having lattice orientations being restricted to high-symmetry cases. This shows that even the relatively weak van der Waals interaction can control the crystalline orientation of the overlayer in a similar way to chemical bonds in covalently bonded semiconductors such as GaAs or Si. Here, the preferred MoS₂ orientation corresponds to the one with the highest commensuration.

While DFT calculations had difficulty explaining the existence of a preferred orientation due to complications related to applying periodic boundary conditions to an incommensurate structure, a remarkably simple model based on pairwise interactions results in predictions in good agreement with the experiment. We believe that this result is general for all vdW heterostructures, and hence we suggest this method as an excellent tool for prediction of such structures.

Local electrical measurements across grain boundaries reveal good stitching between the single crystals in our film with the absence of electrical resistance at most common types of grain boundaries in our sample. The use of sapphire substrates can therefore suppress the formation of tilted grain boundaries, which are detrimental for the electrical properties of the polycrystalline CVD-grown MoS₂.²³ The high quality of our sample is further demonstrated by optical and electrical measurements showing properties superior to exfoliated samples. The high degree of uniformity of our film also allowed optical absorbance measurements to be performed in a broad wavelength range, showing the presence of high-energy absorbance peaks that indicate the suitability of MoS₂ for harvesting the green and blue regions of the solar spectrum and for the fabrication of photodetectors operating in this wavelength range. The proposed growth strategy involving the use of atomically smooth sapphire substrates could pave the way for large-area growth of MoS₂ with high optical and electrical quality retained over large length scales, allowing its use in future electronic and optoelectronic devices.

METHODS

Growth Procedure. Monolayer MoS_2 has been grown by chemical vapor deposition on c-plane sapphire. After consecutive cleaning by acetone/2-propanol/Dl-water and piranha solution,

the substrates were annealed for 1 h at 1000 °C in air. After that, they were placed face-down above a crucible containing $\sim\!5$ mg of MoO₃ ($\geq\!99.998\%$ Alfa Aesar) and loaded into a split-tube three-zone CVD furnace with a 32 mm outer diameter quartz tube. CVD growth was performed at atmospheric pressure



using ultra-high-purity argon as the carrier gas. A second crucible containing 350 mg of sulfur (\geq 99.99% purity, Sigma-Aldrich) was located upstream from the growth substrates. The growth recipe is as follows: set the temperature of 300 °C with 200 sccm for 10 min, ramp to 700 °C with a rate of 50 °C min⁻¹ and 10 sccm of carrier gas flow, set the temperature to 700 °C for 10 min, cool to 570 °C with 10 sccm gas flow, increase the gas flow to 200 sccm, and open the furnace for rapid cooling. For more details, please refer to Supporting Sections 1 and 2.

TEM and AFM Imaging. CVD MoS₂ was transferred from sapphire using the wet transfer KOH method. Samples were first spin coated at 1500 rpm with PMMA A2, resulting in a \sim 100 nm thick polymer film. These were detached in a 30% KOH solution, washed several times in DI water, and transferred onto TEM grids. TEM grids were annealed in the flow of Ar and H₂ for 8 h at 400 °C in order to remove the polymer film. For low-resolution imaging and diffraction studies, 10 nm thick Si₃N₄ windows were used, while for high-resolution TEM (HR-TEM) we used PELCO holey silicon nitride support film with 2.5 um holes in a 200 nm thick Si₃N₄ support. Transmission electron microscopy was performed using a JEOL 2200 FS operated in the 120-200 keV energy range. HR-TEM images were recorded at a magnification of 1 M×. A series of 10-30 images was recorded and stacked with drift correction and averaging using the Stackreg plugin in Fiji (ImageJ). Island orientations in optical images were analyzed using the directionality plugin in Fiji (ImageJ). Samples were also imaged using an atomic force microscope (Asylum Research Cypher) operating in ac mode.

Density Functional Theory Modeling. All ab initio simulations have been performed within density functional theory, using Quantum-ESPRESSO as implemented in PWscf code of the Quantum-ESPRESSO distribution⁴⁸ and VASP. ^{49,50} For calculations using Quantum-ESPRESSO, in order to account for dispersion interactions, we used a revised version⁵¹ of the nonlocal density functional by Vydrov and Van Voorhis⁵² (rVV10). Ionelectron interactions were taken into account by means of ultrasoft pseudopotentials, 53,54 with energy cutoffs of 60 Ry for wave functions and 600 Ry for density. Pseudopotentials have been generated using parameters taken from the PSlibrary repository (v.0.3.0) of the QEforge distribution and setting rPW86^{54,55} as exchange functional and PBE⁵³ as semilocal contribution to the correlation functional, in agreement with the rVV10 parametrization.⁵² Surface calculations were performed by considering Al₂O₃ slabs with six oxygen O₃ layers and 10 (12) aluminum layers in the case of OH (Al) termination. In order to minimize the interaction between periodic replicas, supercells were built including 20 Å of vacuum. Brillouin-zone integration for different supercells was carried out using appropriately converged Monkhorst-Pack grids, corresponding approximately to a gamma-centered 6 \times 6 \times 1 grid for the sapphire surface and $9 \times 9 \times 1$ for MoS₂. The Broyden-Fletcher-Goldfarb-Shanno method was adopted to relax the structures until forces acting on atoms were below 0.025 eV/Å. For calculations using VASP, we have used the density functional theory calculations as implemented in the VASP code ^{49,50} using the PAW approach. ^{56,57} The used functional was the self-consistently implemented vdW-DF⁵⁸⁻⁶⁰ with the optB88 exchange following the results of Mittendorfer et al.61 for graphene adsorption on Ni, where that combination produced results in agreement with RPA calculations and experimental findings. A sufficient number of k-points was used (gammacentered Monkhorst-Pack grid of 3 \times 3 \times 1 for the R0 supercell). An energy cutoff of 500 eV was used along with a 15 Å vacuum spacing between the periodic images in the z-direction, and the dipole correction was applied. 62 The atomic relaxation was performed until the forces dropped below 0.1 meV/Å. The sapphire surface was simulated with the fivelayer-thick slab, of which three top layer were allowed to relax. The top surface was Al terminated.

Kelvin Probe Imaging. For the KPFM measurement an atomic force microscopy system (Asylum Research Cypher) was utilized, allowing the simultaneous measurement of topography and Kelvin voltage with a spatial resolution of about 20 nm and a potential resolution of a few millivolts. We used silicon KPFM probes (Olymups, OMCL-AC240TM) with a nominal radius of

 \sim 30 nm, which were covered with a conductive Ti/Pt (5/20 nm) layer and had a resonance frequency of \sim 70 kHz. An ac modulation voltage (V_{AC}) of 3 V was applied to the probe for the Kelvin probe measurements. An external bias between the two contacts' (source and drain) V_{ds} of 1 V was applied, and the gate voltage V_{g} was typically kept at 0 V. All measurements were performed under ambient conditions.

Optical Characterization. Raman measurements were performed on a commercial system (Jobin-Yvon Horiba LabRam) using a 532 nm laser for excitation. Photoluminescence measurements were performed using a 488 nm laser and a spectrometer (Princeton Instruments SP-2500i) with a liquid nitrogen cooled camera (PiXIS/Pylon/Spec-10:256). Broadband absorbance measurements were performed using a Varian Cary 50 Bio UV—vis spectrophotometer.

Electrical Characterization. CVD-grown single domains of MoS_2 were transferred using PMMA A2 as a support film and etching in 30% KOH onto a degenerately doped Si substrate covered with 270 nm thick SiO_2 . The PMMA film is dissolved in acetone, and residues are removed by annealing in Ar atmosphere at 350 °C for 5 h. PMMA A4 was used as the etching mask during oxygen plasma etching. The devices were annealed at 200 °C in Ar atmosphere to eliminate resist residues and reduce contact resistance.

Conflict of Interest: The authors declare no competing financial interest.

Acknowledgment. Thanks go to D. Walters and J. Cleland from Asylum Research for suggestions related to sapphire surface preparation. We thank R. Gaal for technical assistance with the Raman setup, T. Heine for useful discussions, M. G. Friedl for technical assistance, and A. Allain for help with electrical transport measurements. Device fabrication was carried out in the EPFL Center for Micro/Nanotechnology (CMI). We thank Z. Benes (CMI) for technical support with e-beam lithography and D. Alexander (CIME) for support with electron microscopy, P.L. thanks I. Žutić and the Center for Computational Research, University at Buffalo. M.G. and N.M. acknowledge the Swiss National Supercomputing Centre (CSCS) for simulation time under project ID s337. This work was financially supported by Swiss SNF Sinergia Grant No. 147607, funding from the European Union's Seventh Framework Programme FP7/2007-2013 under Grant Agreement No. 318804 (SNM). Marie Curie ITN network "MoWSeS" (Grant No. 317451), ERC Grant No. 240076, and SNF Grant 135046. We acknowledge funding by the EC under the Graphene Flagship (grant agreement no. 604391). D.D. and D.K. worked on CVD growth. D.D. performed AFM, Raman, and broadband optical characterization, D.O. performed TEM acquisition, data analysis, and longchannel FET fabrication and characterization. D.O. and K.M. worked on Kelvin probe measurements. K.M. fabricated and characterized single-crystal FET devices. P.L. performed DFT calculations using VASP and modeling based on pairwise interactions. M.G. performed DFT calculations using Quantum ESPRESSO. O.L.S. performed PL measurements. M.W.C. performed RHEED acquisition and analysis. Y.C.K. developed and applied the transfer method used for realizing large-area devices. S.B. prepared exfoliated samples for Raman measurements. P.G. supervised Raman measurements, A.F.i.M. supervised PL measurements, A.R. supervised broadband optical measurements, and N.M. supervised DFT calculations performed by M.G. A.K. coordinated and initiated the work. A. F.i.M. contributed to the discussion on the growth mechanisms. All authors performed work on manuscript preparation

Supporting Information Available: Substrate preparation, growth setup, SAED analysis, sapphire-MoS₂ van der Waals interaction, electrical transport measurements on a single crystal, scanning Kelvin probe microscopy, and electrical transport measurements on large-area films. This material is available free of charge via the Internet at http://pubs.acs.org.

REFERENCES AND NOTES

 Novoselov, K. S.; Jiang, D.; Schedin, F.; Booth, T. J.; Khotkevich, V. V.; Morozov, S. V.; Geim, A. K. Two-Dimensional Atomic Crystals. Proc. Natl. Acad. Sci. U.S.A. 2005, 102, 10451–10453.

- Coleman, J. N.; Lotya, M.; O'Neill, A.; Bergin, S. D.; King, P. J.; Khan, U.; Young, K.; Gaucher, A.; De, S.; Smith, R. J.; et al. Two-Dimensional Nanosheets Produced by Liquid Exfoliation of Layered Materials. Science 2011, 331, 568–571.
- 3. Smith, R. J.; King, P. J.; Lotya, M.; Wirtz, C.; Khan, U.; De, S.; O'Neill, A.; Duesberg, G. S.; Grunlan, J. C.; Moriarty, G.; et al. Large-Scale Exfoliation of Inorganic Layered Compounds in Aqueous Surfactant Solutions. *Adv. Mater. (Weinheim, Ger.)* **2011**, *23*, 3944–3948.
- Kam, K. K.; Parkinson, B. A. Detailed Photocurrent Spectroscopy of the Semiconducting Group Vib Transition Metal Dichalcogenides. J. Phys. Chem. 1982, 86, 463–467.
- Lebegue, S.; Eriksson, O. Electronic Structure of Two-Dimensional Crystals from ab Initio Theory. *Phys. Rev. B* 2009, 79, 115409.
- Splendiani, A.; Sun, L.; Zhang, Y.; Li, T.; Kim, J.; Chim, C.-Y.; Galli, G.; Wang, F. Emerging Photoluminescence in Monolayer MoS₂. Nano Lett. 2010, 10, 1271–1275.
- Mak, K. F.; Lee, C.; Hone, J.; Shan, J.; Heinz, T. F. Atomically Thin MoS₂: A New Direct-Gap Semiconductor. *Phys. Rev. Lett.* 2010, 105, 136805.
- Kuc, A.; Zibouche, N.; Heine, T. Influence of Quantum Confinement on the Electronic Structure of the Transition Metal Sulfide TS₂. Phys. Rev. B 2011, 83, 245213.
- Lee, C.; Yan, H.; Brus, L. E.; Heinz, T. F.; Hone, J.; Ryu, S. Anomalous Lattice Vibrations of Single- and Few-Layer MoS₂. ACS Nano 2010, 4, 2695–2700.
- Benameur, M. M.; Radisavljevic, B.; Heron, J. S.; Sahoo, S.; Berger, H.; Kis, A. Visibility of Dichalcogenide Nanolayers. Nanotechnology 2011, 22, 125706.
- Bertolazzi, S.; Krasnozhon, D.; Kis, A. Nonvolatile Memory Cells Based on MoS₂/Graphene Heterostructures. ACS Nano 2013, 7, 3246–3252.
- Lopez-Sanchez, O.; Lembke, D.; Kayci, M.; Radenovic, A.; Kis, A. Ultrasensitive Photodetectors Based on Monolayer MoS₂. Nat. Nanotechnol. 2013, 8, 497–501.
- Yin, Z.; Li, H.; Li, H.; Jiang, L.; Shi, Y.; Sun, Y.; Lu, G.; Zhang, Q.; Chen, X.; Zhang, H. Single-Layer MoS₂ Phototransistors. ACS Nano 2012, 6, 74–80.
- Liu, K.; Feng, J. D.; Kis, A.; Radenovic, A. Atomically Thin Molybdenum Disulfide Nanopores with High Sensitivity for DNA Trans Location. ACS Nano 2014, 8, 2504–2511.
- Bertolazzi, S.; Brivio, J.; Kis, A. Stretching and Breaking of Ultrathin MoS₂. ACS Nano 2011, 5, 9703–9709.
- Chang, H.-Y.; Yang, S.; Lee, J.; Tao, L.; Hwang, W.-S.; Jena, D.; Lu, N.; Akinwande, D. High-Performance, Highly Bendable MoS₂ Transistors with High-K Dielectrics for Flexible Low-Power Systems. ACS Nano 2013, 7, 5446–5452.
- Schäfer, H. Chemical Transport Reactions; Academic Press: New York, 1964.
- Liu, K.-K.; Zhang, W.; Lee, Y.-H.; Lin, Y.-C.; Chang, M.-T.; Su, C.-Y.; Chang, C.-S.; Li, H.; Shi, Y.; Zhang, H.; et al. Growth of Large-Area and Highly Crystalline MoS₂ Thin Layers on Insulating Substrates. Nano Lett. 2012, 12, 1538–1544.
- Zhan, Y.; Liu, Z.; Najmaei, S.; Ajayan, P. M.; Lou, J. Large-Area Vapor-Phase Growth and Characterization of MoS₂ Atomic Layers on a SiO₂ Substrate. Small 2012, 8, 966–971.
- Lee, Y.-H.; Zhang, X.-Q.; Zhang, W.; Chang, M.-T.; Lin, C.-T.; Chang, K.-D.; Yu, Y.-C.; Wang, J. T.-W.; Chang, C.-S.; Li, L.-J.; et al. Synthesis of Large-Area MoS₂ Atomic Layers with Chemical Vapor Deposition. Adv. Mater. (Weinheim, Ger.) 2012, 24, 2320–2325.
- Najmaei, S.; Liu, Z.; Zhou, W.; Zou, X.; Shi, G.; Lei, S.; Yakobson, B. I.; Idrobo, J.-C.; Ajayan, P. M.; Lou, J. Vapour Phase Growth and Grain Boundary Structure of Molybdenum Disulphide Atomic Layers. *Nat. Mater.* 2013, 12, 754–759
- van der Zande, A. M.; Huang, P. Y.; Chenet, D. A.; Berkelbach, T. C.; You, Y.; Lee, G.-H.; Heinz, T. F.; Reichman, D. R.; Muller, D. A.; Hone, J. C. Grains and Grain Boundaries in Highly Crystalline Monolayer Molybdenum Disulphide. *Nat. Mater.* 2013, 12, 554–561.
- 23. Najmaei, S.; Amani, M.; Chin, M. L.; Liu, Z.; Birdwell, A. G.; O'Regan, T. P.; Ajayan, P. M.; Dubey, M.; Lou, J. Electrical

- Transport Properties of Polycrystalline Monolayer Molybdenum Disulfide. ACS Nano **2014**, 8, 7930–7937.
- 24. Yazyev, O. V.; Chen, Y. P. Polycrystalline Graphene and Other Two-Dimensional Materials. *Nat. Nanotechnol.* **2014**, *9*, 755–767.
- Koma, A. Van Der Waals Epitaxy for Highly Lattice-Mismatched Systems. J. Cryst. Growth 1999, 201, 236–241.
- Bakti Utama, M. I.; Zhang, Q.; Zhang, J.; Yuan, Y.; Belarre, F. J.; Arbiol, J.; Xiong, Q. Recent Developments and Future Directions in the Growth of Nanostructures by Van Der Waals Epitaxy. Nanoscale 2013, 5, 3570–3588.
- Ji, Q.; Zhang, Y.; Gao, T.; Zhang, Y.; Ma, D.; Liu, M.; Chen, Y.; Qiao, X.; Tan, P.-H.; Kan, M.; et al. Epitaxial Monolayer MoS₂ on Mica with Novel Photoluminescence. Nano Lett. 2013, 13. 3870–3877.
- Shi, Y.; Zhou, W.; Lu, A.-Y.; Fang, W.; Lee, Y.-H.; Hsu, A. L.; Kim, S. M.; Kim, K. K.; Yang, H. Y.; Li, L.-J.; et al. Van Der Waals Epitaxy of MoS₂ Layers Using Graphene as Growth Templates. Nano Lett. 2012, 12, 2784–2791.
- Ago, H.; Endo, H.; Solís-Fernández, P.; Takizawa, R.; Ohta, Y.; Fujita, Y.; Yamamoto, K.; Tsuji, M. Controlled Van Der Waals Epitaxy of Monolayer MoS₂ Triangular Domains on Graphene. ACS Appl. Mater. Interfaces 2015, 7, 5265–5273.
- Lin, Y.-C.; Lu, N.; Perea-Lopez, N.; Li, J.; Lin, Z.; Peng, X.; Lee, C. H.; Sun, C.; Calderin, L.; Browning, P. N.; et al. Direct Synthesis of Van Der Waals Solids. ACS Nano 2014, 8, 3715–3723.
- Gonschorek, M.; Carlin, J.-F.; Feltin, E.; Py, M. A.; Grandjean,
 N. High Electron Mobility Lattice-Matched Alinn/Gan
 Field-Effect Transistor Heterostructures. Appl. Phys. Lett.
 2006, 89, -.
- 32. Yu, Y.; Li, C.; Liu, Y.; Su, L.; Zhang, Y.; Cao, L. Controlled Scalable Synthesis of Uniform, High-Quality Monolayer and Few-Layer MoS₂ Films. *Sci. Rep.* **2013**, *3*.
- Zhang, Y.; Zhang, Y.; Ji, Q.; Ju, J.; Yuan, H.; Shi, J.; Gao, T.; Ma, D.; Liu, M.; Chen, Y.; et al. Controlled Growth of High-Quality Monolayer WS₂ Layers on Sapphire and Imaging Its Grain Boundary. ACS Nano 2013, 7, 8963–8971.
- Yoshimoto, M.; Maeda, T.; Ohnishi, T.; Koinuma, H.; Ishiyama, O.; Shinohara, M.; Kubo, M.; Miura, R.; Miyamoto, A. Atomic-Scale Formation of Ultrasmooth Surfaces on Sapphire Substrates for High-Quality Thin-Film Fabrication. *Appl. Phys. Lett.* 1995, 67, 2615–2617.
- Curiotto, S.; Chatain, D. Surface Morphology and Composition of C-, a- and M-Sapphire Surfaces in O₂ and H₂ Environments. Surf. Sci. 2009, 603, 2688–2697.
- Lauritsen, J. V.; Kibsgaard, J.; Helveg, S.; Topsoe, H.; Clausen,
 B. S.; Laegsgaard, E.; Besenbacher, F. Size-Dependent Structure of MoS₂ Nanocrystals. *Nat. Nanotechnol.* 2007, 2.53–58.
- Brivio, J.; Alexander, D. T. L.; Kis, A. Ripples and Layers in Ultrathin MoS₂ Membranes. *Nano Lett.* 2011, 11, 5148– 5153.
- Chakraborty, B.; Bera, A.; Muthu, D. V. S.; Bhowmick, S.; Waghmare, U. V.; Sood, A. K. Symmetry-Dependent Phonon Renormalization in Monolayer MoS₂ Transistor. *Phys. Rev. B* **2012**, *85*, 161403.
- Islam, M. R.; Kang, N.; Bhanu, U.; Paudel, H. P.; Erementchouk, M.; Tetard, L.; Leuenberger, M. N.; Khondaker, S. I. Tuning the Electrical Property via Defect Engineering of Single Layer MoS₂ by Oxygen Plasma. Nanoscale 2014, 6, 10033– 10039.
- Plechinger, G.; Mann, J.; Preciado, E.; Barroso, D.; Nguyen, A.; Eroms, J.; Schüller, C.; Bartels, L.; Korn, T. A Direct Comparison of CVD-Grown and Exfoliated MoS₂ Using Optical Spectroscopy. Semicond. Sci. Technol. 2014, 29, 064008.
- Klots, A. R.; Newaz, A. K. M.; Wang, B.; Prasai, D.; Krzyzanowska, H.; Caudel, D.; Ghimire, N. J.; Yan, J.; Ivanov, B. L.; Velizhanin, K. A.; et al. Probing Excitonic States in Ultraclean Suspended Two-Dimensional Semiconductors by Photocurrent Spectroscopy.arXiv:1403.6455.
- Britnell, L.; Ribeiro, R. M.; Eckmann, A.; Jalil, R.; Belle, B. D.; Mishchenko, A.; Kim, Y.-J.; Gorbachev, R. V.; Georgiou, T.; Morozov, S. V.; et al. Strong Light-Matter Interactions in

- Heterostructures of Atomically Thin Films. *Science* **2013**, *340*, 1311–1314.
- 43. Geim, A. K.; Grigorieva, I. V. Van Der Waals Heterostructures. *Nature* **2013**, *499*, 419–425.
- 44. Schmidt, H.; Wang, S.; Chu, L.; Toh, M.; Kumar, R.; Zhao, W.; Castro Neto, A. H.; Martin, J.; Adam, S.; Özyilmaz, B.; et al. Transport Properties of Monolayer MoS₂ Grown by Chemical Vapor Deposition. Nano Lett. 2014, 14, 1909– 1913.
- Radisavljevic, B.; Kis, A. Mobility Engineering and a Metal-Insulator Transition in Monolayer MoS₂. Nat. Mater. 2013, 12. 815–820.
- Baugher, B.; Churchill, H. O. H.; Yang, Y.; Jarillo-Herrero, P. Intrinsic Electronic Transport Properties of High Quality Monolayer and Bilayer MoS₂. Nano Lett. 2013, 13, 4212– 4216
- Nonnenmacher, M.; Oboyle, M. P.; Wickramasinghe, H. K. Kelvin Probe Force Microscopy. Appl. Phys. Lett. 1991, 58, 2921–2923.
- Paolo, G.; Stefano, B.; Nicola, B.; Matteo, C.; Roberto, C.; Carlo, C.; Davide, C.; Guido, L. C.; Matteo, C.; Ismaila, D.; et al. Quantum Espresso: A Modular and Open-Source Software Project for Quantum Simulations of Materials. J. Phys.: Condens. Matter 2009, 21, 395502.
- 49. Blöchl, P. E. Projector Augmented-Wave Method. *Phys. Rev. B* **1994**, *50*, 17953–17979.
- Kresse, G.; Joubert, D. From Ultrasoft Pseudopotentials to the Projector Augmented-Wave Method. *Phys. Rev. B* 1999, 59, 1758–1775.
- Sabatini, R.; Gorni, T.; de Gironcoli, S. Nonlocal Van Der Waals Density Functional Made Simple and Efficient. *Phys. Rev. B* 2013, 87, 041108.
- Vydrov, O. A.; Van Voorhis, T. Nonlocal Van Der Waals Density Functional: The Simpler the Better. J. Chem. Phys. 2010, 133, 244103.
- Perdew, J. P.; Burke, K.; Ernzerhof, M. Generalized Gradient Approximation Made Simple. *Phys. Rev. Lett.* 1996, 77, 3865–3868.
- Murray, É. D.; Lee, K.; Langreth, D. C. Investigation of Exchange Energy Density Functional Accuracy for Interacting Molecules. J. Chem. Theory Comput. 2009, 5, 2754– 2762.
- Perdew, J. P.; Yue, W. Accurate and Simple Density Functional for the Electronic Exchange Energy: Generalized Gradient Approximation. *Phys. Rev. B* 1986, 33, 8800–8802.
- Kresse, G.; Furthmüller, J. Efficient Iterative Schemes for ab Initio Total-Energy Calculations Using a Plane-Wave Basis Set. Phys. Rev. B 1996, 54, 11169–11186.
- 57. Kresse, G.; Hafner, J. Ab Initio Molecular Dynamics for Liquid Metals. Phys. Rev. B 1993, 47, 558–561.
- Dion, M.; Rydberg, H.; Schröder, E.; Langreth, D. C.; Lundqvist, B. I. Van Der Waals Density Functional for General Geometries. *Phys. Rev. Lett.* 2004, 92, 246401.
- Klimeš, J.; Bowler, D. R.; Michaelides, A. Chemical Accuracy for the Van Der Waals Density Functional. J. Phys.: Condens. Matter 2010, 22, 022201.
- Klimeš, J.; Bowler, D. R.; Michaelides, A. Van Der Waals Density Functionals Applied to Solids. *Phys. Rev. B* 2011, 83, 195131.
- Mittendorfer, F.; Garhofer, A.; Redinger, J.; Klimeš, J.; Harl, J.; Kresse, G. Graphene on Ni(111): Strong Interaction and Weak Adsorption. *Phys. Rev. B* 2011, 84, 201401.
- Neugebauer, J.; Scheffler, M. Adsorbate-Substrate and Adsorbate-Adsorbate Interactions of Na and K Adlayers on Al(111). Phys. Rev. B 1992, 46, 16067–16080.

Supplementary Information

for

Large-Area Epitaxial Monolayer MoS₂

Dumitru Dumcenco^{1†}, Dmitry Ovchinnikov^{1†}, Kolyo Marinov^{1†}, Predrag Lazić², Marco Gibertini³, Nicola Marzari³, Oriol Lopez Sanchez¹, Yen-Cheng Kung¹, Daria Krasnozhon¹, Ming-Wei Chen¹, Simone Bertolazzi¹, Philippe Gillet⁴, Anna Fontcuberta i Morral³, Aleksandra Radenovic⁵, Andras Kis^{1*}

¹Electrical Engineering Institute, Ecole Polytechnique Federale de Lausanne (EPFL), CH-1015 Lausanne, Switzerland

²Institute Ruđer Bošković (IRB), HR-10000 Zagreb, Croatia ³Institute of Materials, Ecole Polytechnique Federale de Lausanne (EPFL), CH-1015 Lausanne, Switzerland

⁴Institute of Condensed Matter Physics, Ecole Polytechnique Federale de Lausanne (EPFL), CH-1015 Lausanne, Switzerland

⁵Institute of Bioengineering, Ecole Polytechnique Federale de Lausanne (EPFL), CH-1015 Lausanne, Switzerland

[†]These authors contributed equally *Correspondence should be addressed to: Andras Kis, <u>andras.kis@epfl.ch</u>

1. Substrate preparation

The preparation of atomically smooth terraces on the sapphire surface is critical to achieving control over lattice orientation during CVD growth.

We start with commercially available EPI grade polished c-plane sapphire (University Wafers) which is first diced into 1 cm × 1 cm dies. An AFM image of the as-received substrate with the corresponding height histogram from a 500 nm \times 500 nm area is shown on Figure S1a. The surface is relatively smooth, with the height histogram showing a standard deviation $\sigma = 154$ pm, lower than for typical SiO₂ surfaces ($\sigma \sim 300$ pm). The sapphire dies are loaded in a quartz tube and annealed in a tube furnace in air for 1h at 1000 °C prior to the growth run. Following the annealing procedure, the samples are allowed to cool to room temperature in air before we place them in the CVD growth furnace. An AFM image of the surface after annealing is shown on Figure S1b and demonstrates the dramatic change in surface morphology during annealing. The resulting surface shows atomically flat surfaces with atomic steps due to the small miscut induced during the cutting of the sapphire boule. Based on the height histogram, we extract a step size ~ 2.1 Å and a terrace width ~ 70 nm. Terraces are atomically smooth, with a surface roughness $\sigma = 33$ pm. This height variation is smaller than the diameters of oxygen, aluminum or sulphur atoms (122 pm, 242 pm and 205 pm respectively). Such atomically smooth surfaces allow the van der Waals interaction between sapphire and MoS₂ to control the lattice orientation during the CVD growth of monolayer MoS₂.

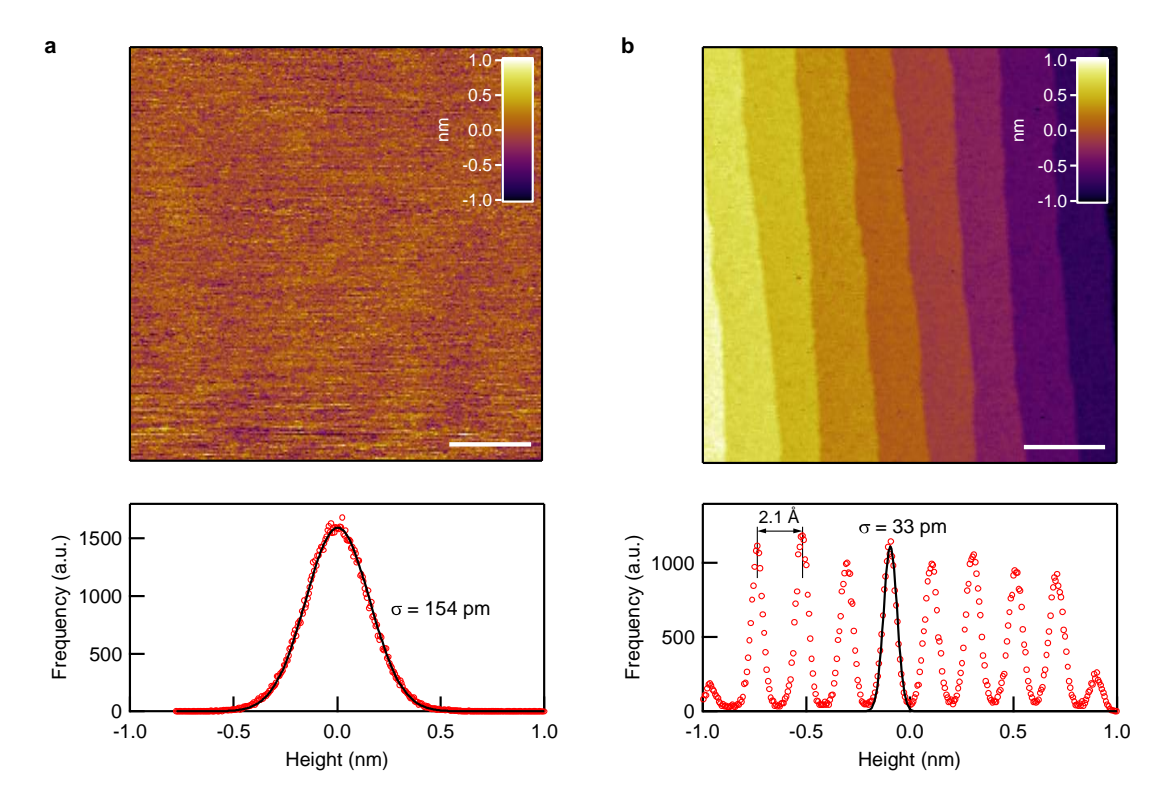


Figure S1. Effect of annealing in air on the morphology of c-plane sapphire. a, AFM image of the as received sapphire surface. Top panel: AFM image. Bottom panel: height histogram with a Gaussian fit showing a standard deviation σ = 154 pm. b, AFM image of annealed sapphire used here as the growth substrate. After annealing in air, the surface shows atomically smooth terraces. Top panel: AFM image. Bottom panel: height histogram with a Gaussian fit showing a standard deviation σ = 33 pm and a terrace height ~ 2.1 Å. The color scales in a and b are the same (2 nm). The scale bars are 100 nm long.

The importance of surface annealing can also be seen on Figure S2 where we show an optical image and orientation histogram for CVD MoS₂ on a sapphire sample which was not annealed. Using a surface without the annealing treatment results in a wide distribution of single crystal orientations (Figure S2a), as seen on the associated orientation histogram (Figure S2b). A relatively large number of particles, presumably growth seeds can also be seen.

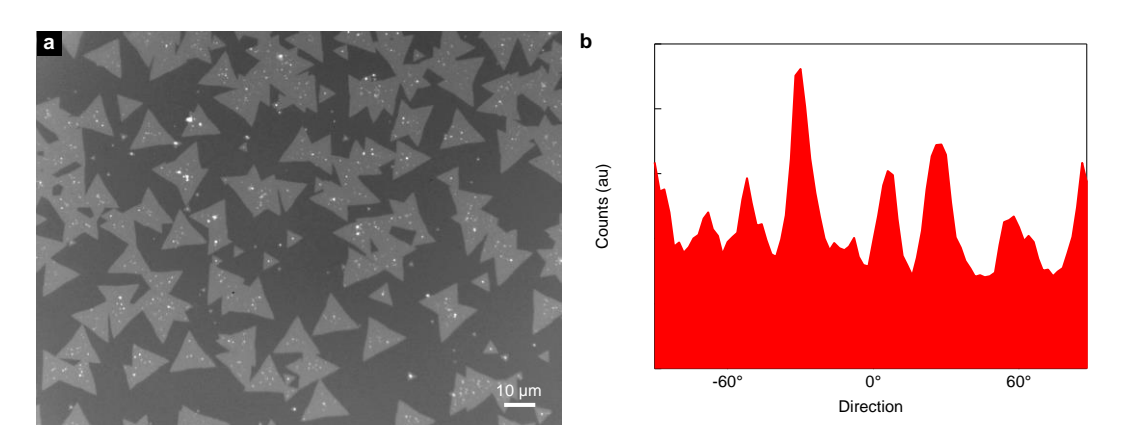


Figure S2. Effect of sapphire surface annealing on the lattice orientation of CVD-grown MoS_2 . a, Optical image of a triangular MoS_2 single crystals grown on sapphire without annealing. b, Orientation histogram obtained from the optical image in a.

2. Growth setup

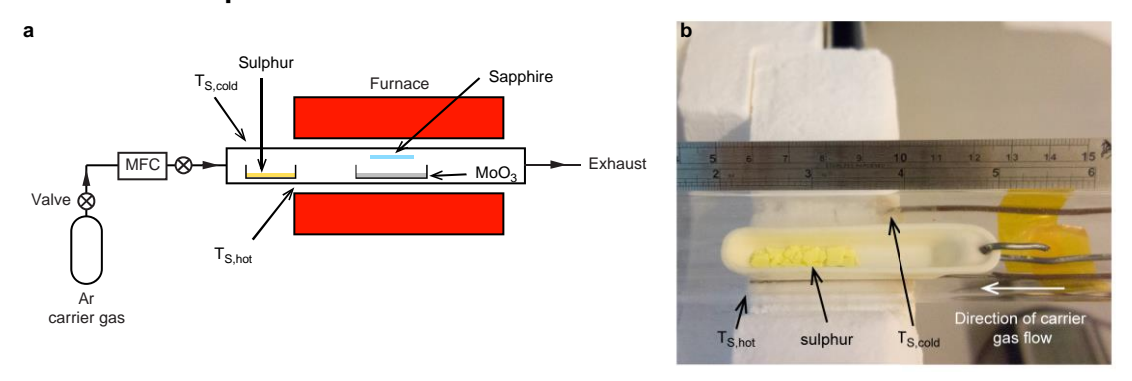


Figure S3. Schematic of the growth system a, Schematic drawing of the growth system. b, Sulphur pieces are loaded in an alumina boat placed at the end of the heated section of the split-tube three zone furnace. All three zones of the furnace are maintained at the same temperature. The boat stays in the same place during the entire growth run. The temperature at the two different points $T_{S,\text{bol}}$ and $T_{S,\text{cold}}$ is measured using a thermocouple.

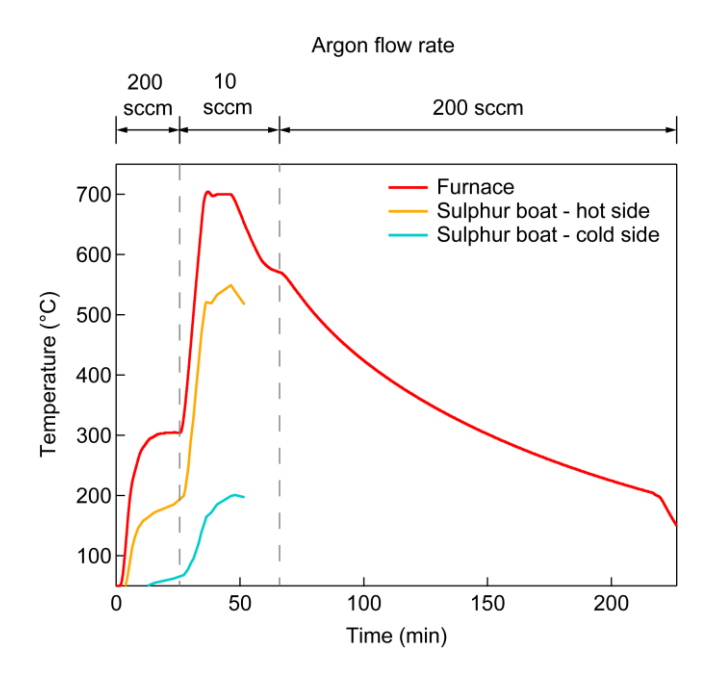


Figure S4. Time dependence of growth parameters. Temperature and argon carrier gas flow rate as a function of time. The system is maintained at atmospheric pressure during the entire growth run.

3. SAED analysis

To further investigate the relative crystalline orientations of triangles on a large scale, the alignment of their diffraction pattern has been used. The alignment of triangles on the macro scale is clearly visible optically (Figure 1b,c) and confirmed by the orientation histogram (Figure 1f). Using select-area electron diffraction (SAED), we perform a more precise determination of triangle alignment by probing the changes of diffraction patterns and related lattice rotations of different triangles. Multiple SAED patterns have been recorded from different locations on the sample. A low-resolution TEM (LR-TEM) micrograph (Figure S5a) and related representative SAED patterns (Figure S5 b-e) are presented on Figure S5. The diffraction pattern alignment of two pairs of triangles (1-3 and 2-4) is evident. Moreover, red lines in parts b-e are parallel, indicating that these triangles have the same lattice orientation.

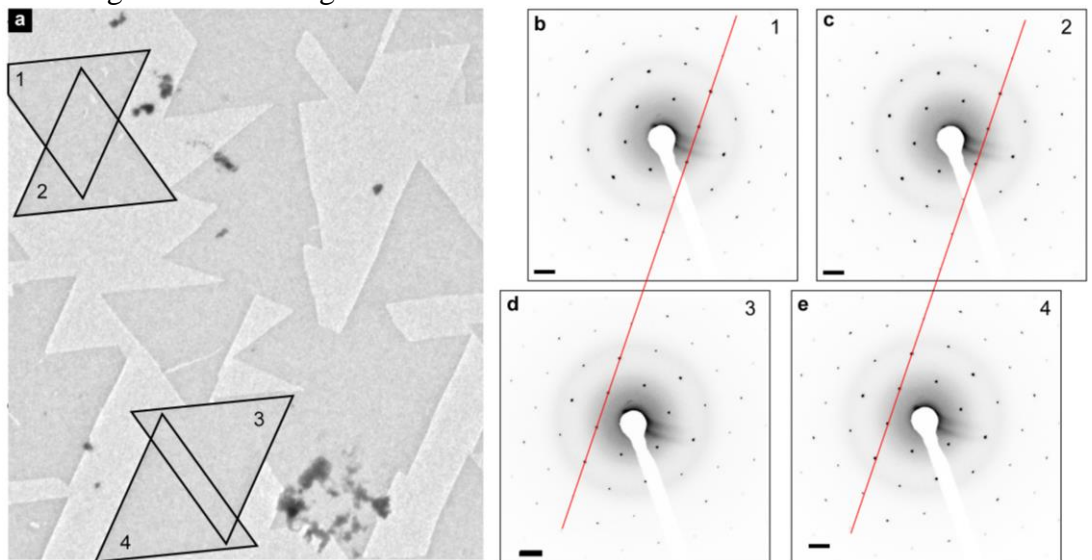


Figure S5. SAED study of crystalline orientations of CVD MoS₂. a, LR-TEM micrograph of several merging triangles. Scale bar - 5 µm. Two pairs of selected triangles are highlighted. **b-e,** SAED diffraction patterns acquired on triangles labeled 1-4 in part a. Scale bar: 2 nm⁻¹. Parallel red lines are provided as a guide for tracking the relative orientations of diffraction patterns.

Furthermore, we have performed measurements on several triangles to precisely identify the orientation of the crystalline lattice with respect to the triangle orientation. The key to identifying these orientations is the comparison of intensities of the first family of diffraction spots [-1100]. The lattice of MoS_2 consists of two sublattices - Mo and S, which results in small differences of intensities in the [-1100] family of diffraction spots in the single-layer limit because of inversion symmetry breaking, as confirmed previously experimentally by correlation between diffraction patterns and HR-TEM micrographs, as well as by modeling. Lower-intensity diffraction correspond to the sulfur sublattice.

Figure S6 presents merged triangles rotated by 180° with respect to each other. On Figure S6a a micrograph showing merged triangles with the opposite geometrical orientation is presented. We mark the triangles Triangle 1 and Triangle 2 and further inspect each triangle separately using SAED.

Figure S6b presents the SAED pattern of Triangle 1. Furthermore, we analyze the intensities in the [-1100] diffraction spot family. To illustrate the relationship between the intensities of diffraction spots inside the [-1100] family, we plot the profile along the red line, with the corresponding intensities plotted on part Figure S6d. The same

analysis for Triangle 2 is shown on Figures S6c and e. We mark with blue and red the spots corresponding to the Mo and S sublattices. We find that the lattices in the two triangles are also rotated by 180°. All the triangles we examined showed the same asymmetry in SAED spot intensities, indicating that same relationship between triangle edge and lattice orientation, shown on Figure S6a.

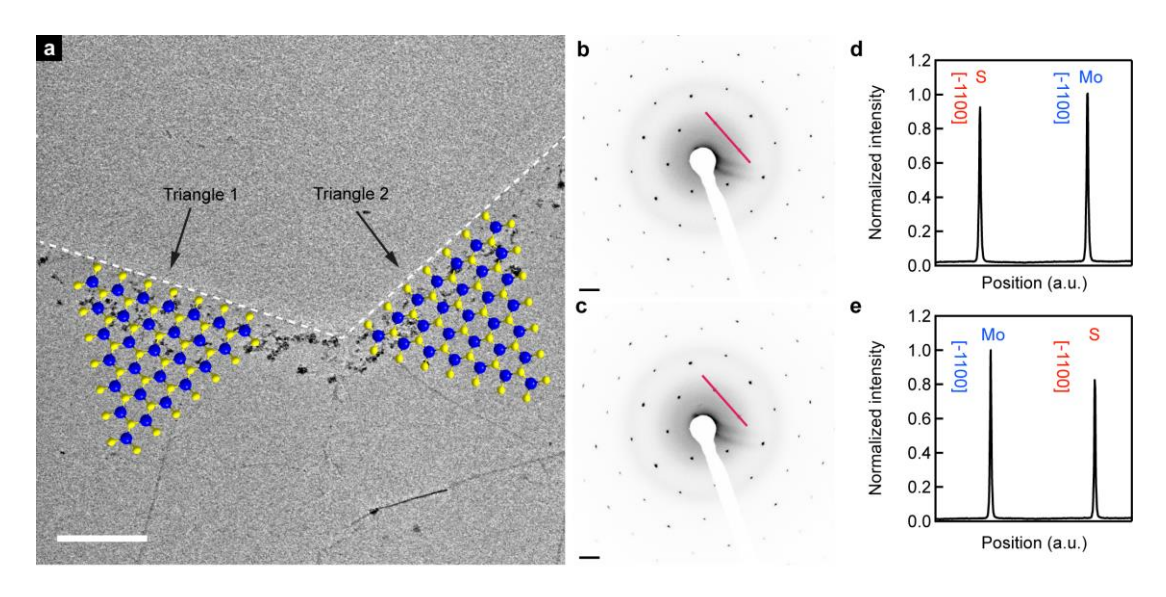


Figure S6. SAED study of crystalline orientations of CVD MoS₂. a, TEM micrograph of two merging triangles of CVD MoS₂ rotated by 180°. The overlaid structural model is for illustration only. Scale bar - 0.5 µm. **b,** SAED pattern acquired on Triangle 1. Scale bar 2 nm⁻¹. **c,** Same as b but for Triangle 2. Scale bar - 2 nm⁻¹. **d,** Diffraction spot intensity plotted along the red line in **b** for Triangle 1. **e,** Diffraction spot intensity plotted along the red line in **c** for Triangle 2.

4. Calculations of the sapphire-MoS₂ van der Waals interaction

In order to perform first-principles simulations of MoS_2 on the surface of Al_2O_3 within periodic boundary conditions, we need to define a supercell (the coincident site lattice) that can accommodate both lattices, allowing for a relative rotation between them by an angle θ , and possibly for some small strain in the monolayer. This corresponds to assuming that van der Waals interactions are sufficiently strong to enforce commensurability between MoS_2 and the underlying sapphire surface. We start from the unit cells of the MoS_2 and sapphire, shown in Figure S7.

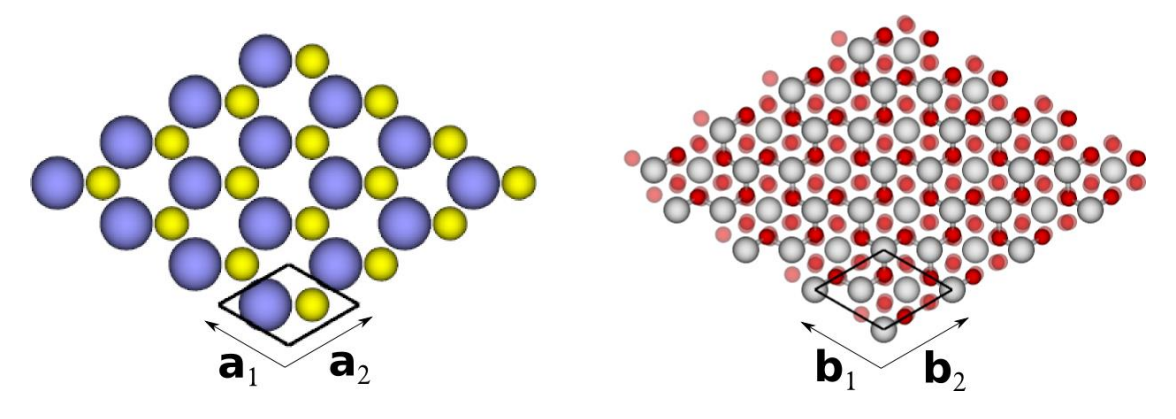


Figure S7. Unit cells of single-layer MoS₂ (left) and 5-layers Al₂O₃ sapphire (right).

Since both lattices are hexagonal, the supercell will also be hexagonal with a primitive lattice vector C that can be written as

$$\mathbf{C} = n_1 \, \mathbf{a}_1 + n_2 \, \mathbf{a}_2 = (1 + \epsilon) \, R_{\theta} (m_1 \, \mathbf{b}_1 + m_2 \, \mathbf{b}_2). \tag{1}$$

Here a_1 , a_2 and b_1 , b_2 are the primitive lattice vectors of the sapphire surface and MoS₂ respectively, n_1 , n_2 and m_1 , m_2 are integers, and R_{θ} and ϵ are the rotation and strain to be applied to MoS₂. The size L=|C| of the supercell can thus assume only discrete values, and each supercell is identified by a set of integers $(n_1, n_2; m_1, m_2)$ for which there always exists a couple (θ, ϵ) so that Eq. (1) is satisfied.

In Figure S8. we consider for instance a supercell identified by (2,1;3,1). This corresponds in Wood's notation³ to a $\sqrt{3} \times \sqrt{3} R 30^{\circ}$ supercell for sapphire and a $\sqrt{7} \times \sqrt{7} R 19.11^{\circ}$ supercell for MoS₂. The supercell size is L = 8.34 Å and in order to satisfy Eq. (1) we need to strain the MoS₂ lattice by 1.9% ($\varepsilon = 0.019$) and to introduce a relative rotation by $\theta \simeq 10.89^{\circ}$ between sapphire and MoS₂. In Figure S8. we report the relative rotation angle θ as a function of size L for all possible supercells for which the strain we need to apply to MoS₂ (represented by the color coding) is smaller than 5%. For simplicity we considered only angles $0^{\circ} < \theta < 60^{\circ}$, since any other angle corresponds either to the same structure by symmetry or to a structure obtained by applying inversion to MoS₂.

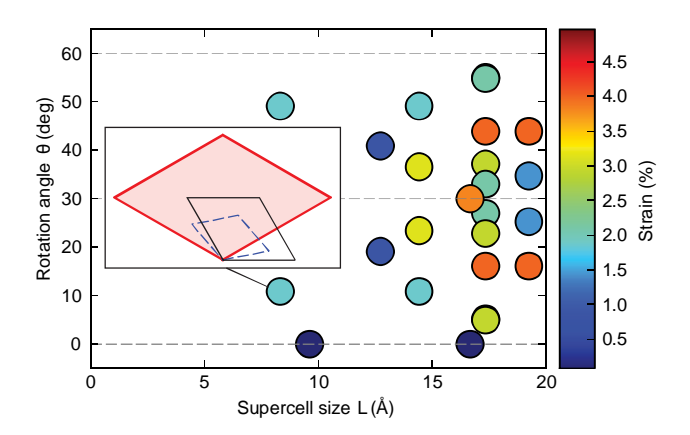


Figure S8. Graphical representation of possible supercells for MoS_2 on sapphire. Each circle denotes a supercell, characterized by its size L, the relative rotation angle θ , and the strain which has to be applied to MoS_2 in order to fulfill Eq. (1) and here represented by the color coding. The inset shows an example of supercell (red shaded area) corresponding to the set of integers (2,1;3,1) (see text). In this case an angle $\theta \simeq 10.89^\circ$ is present between the primitive cell of MoS_2 (blue dashed line) and that of the sapphire surface (black solid line).

In addition to the relative orientation of the unit cells, there is an additional degree of freedom related to the relative shift between the MoS_2 and sapphire lattices. To determine influence of that factor we have generated 3 nonequivalent MoS_2 layer positions for one relative orientation of the unit cells (the 0 orientation). Representative examples of cells used for calculation are shown in Figure S9.

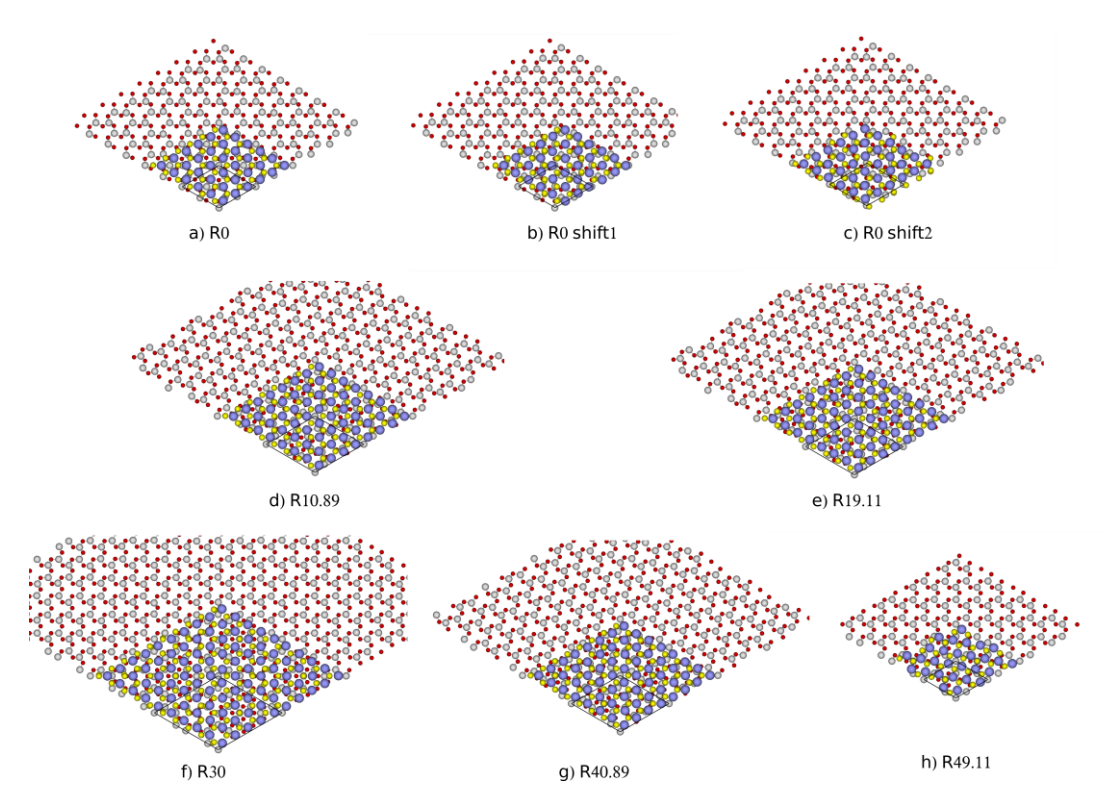


Figure S9. Representative examples of generated common supercells. Rotation angle of MoS_2 unit cell is given as x (in Rx). MoS_2 is shown only partially covering the surface so that underlying Al_2O_3 structure is visible as well (only the last layer is shown). For the R0 cell, three different relative positions of MoS_2 with respect to sapphire are shown.

The main results of binding energies between MoS_2 and Al_2O_3 are given in Table 1. for the five smallest supercells with a strain smaller than 5%, together with the corresponding values of L, θ , and ϵ . Results are also reported for the smallest supercell with $\theta=30^\circ$. The binding energy is defined as the energy difference between the relaxed system and the system parts - i.e. calculations of the self-standing MoS_2 slab are done with the strained slab. The influence of strain is discussed further in the text.

We also compared two different codes and functionals: the PWscf code of the Quantum-ESPRESSO distribution 4 with a revised version 5 of the non-local density functional by Vydrov and Van Voorhis 6 (rVV10) and VASP, $^{7.8}$ using PAW datasets $^{9, 10}$ and vdW-DF $^{11,12, 13}$ with opt88.

We present here the results obtained using the Quantum-ESPRESSO code; results for VASP are closely similar. The binding energies for the five smallest supercells with a strain smaller that 5% are given in Table 1, together with the corresponding values of L, θ , and ϵ . Results are also reported for two supercells with $\theta = 30^{\circ}$.

		Supercell					
Supercell size <i>L</i>		8.34 Å	8.34 Å	9.63 Å	12.74 Å	12.74 Å	16.68 Å
Rotation angle θ		49.11°	10.89°	0°	19.11°	40.89°	30°
Strain ϵ		1.9%	1.9%	0.1%	0.9%	0.9%	3.8%
Binding	Al	-256 (-290)	-256 (-290)	-296 (-296)	-285 (-292)	-285 (-292)	-196 (-315)
Energy (meV/MoS ₂ Unit)	ОН	-185 (-218)	-184 (-218)	-224 (-224)	-215 (-223)	-214 (-222)	-116 (-236)

Table 1. Geometrical parameters and binding energies (in meV per MoS_2 unit) corresponding to different supercells of MoS_2 on sapphire with Al and OH surface termination. The values in parenthesis are binding energies after subtracting the elastic contribution due to the strain on MoS_2 . Supercell sizes and strains have been obtained using the calculated equilibrium lattice constants of the sapphire surface (4.814 Å) and of MoS_2 (3.212 Å). Calculations were performed using the PWscf code of the Quantum-ESPRESSO distribution⁴ with a revised version⁵ of the non-local density functional by Vydrov and Van Voorhis⁶ (rVV10).

First, we note that the binding energy is always negative and, for a given supercell size, does not depend on the rotation angle. Moreover, although the Al surface is more reactive and binds more strongly the MoS_2 layer by almost 70 meV/MoS_2 unit, the relative stability of different supercells is very similar for both surface terminations. In particular, the supercell corresponding to perfectly aligned lattices (i.e. $\theta = 0^{\circ}$) is the most stable one by approximately 10 meV/MoS_2 unit. Nonetheless, we do not find a subdominant orientation rotated by 30° . The supercell corresponding to $\theta = 30^{\circ}$ turns out to be unfavourable, although this is mainly due to the large strain that is necessary to apply to MoS_2 in order to have commensurability.

This condition, on the other hand, is not completely justified, as van der Waals interactions typically do not force the epilayer to be exactly commensurate with the substrate. It is thus important to estimate the binding energy in the case of incommensurate growth of MoS₂ on sapphire. To a first approximation, this could be done by subtracting from the binding energies in Table 1 the contribution due to the elastic energy associated with the strain on MoS2 that we introduced to satisfy the commensurability condition. We stress that values obtained in this way represent upper bounds to the true binding energy. Indeed, in a truly incommensurate situation we would not have the perfect registry between substrate and MoS2 that we impose in the underlying commensurate calculation. This effect is more significant for highly incommensurate orientations (e.g., $\theta = 30^{\circ}$) when ϵ is larger. In Table 1, we show in parenthesis the binding energies obtained by using the equation of state of MoS₂ to estimate the elastic contribution. We note that in this case the $\theta = 30^{\circ}$ orientation is the most stable one by 12 (19) meV/MoS₂ unit for OH (Al) termination. A more conclusive statement on the relative stability between the two is not feasible, owing to a possible overestimation of the binding energy for $\theta = 30^{\circ}$.

To put binding energies in perspective, we can compare them with the binding energy of graphene layers in bulk graphite, which is of almost pure van der Waals nature and is 50 meV per carbon atom which is equivalent to 0.303 J/m^2 . For MoS₂, 296 meV/MoS_2 unit is equivalent to 0.537 J/m^2 .

In order to further explore the nature of interaction, we have visualized the charge transfer by calculating the charge density difference between the system and its parts as well as visualizing the nonlocal correlation binding energy which gives rise to van der Waals interaction. The definition of the nonlocal correlation binding energy is given in ref. 14 while a very recent physical interpretation of the nature of nonlocal correlation binding energy can be found in ref. 15

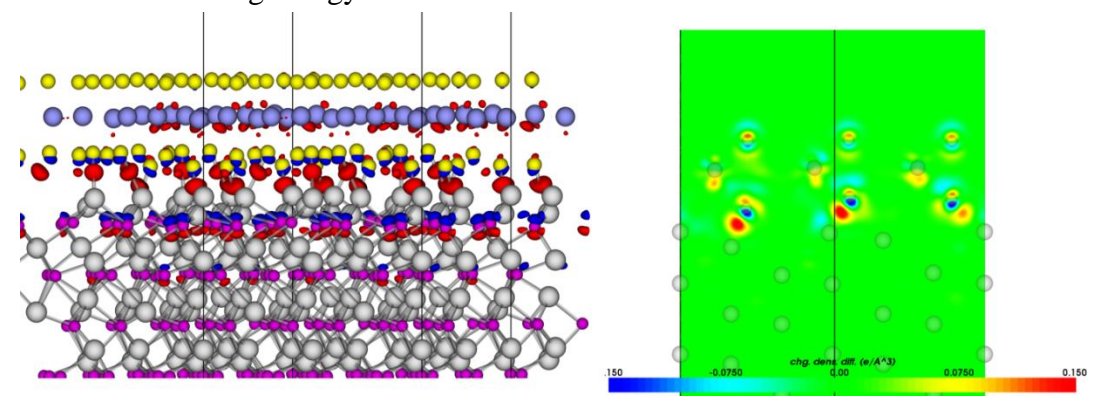


Figure S10. Charge density difference for the R0(a) supercell. Isosurfaces (left) for the values 0.1 (red) and -0.1 e/ \mathring{A}^3 (blue) are shown. Cross-section in the plane along the longer diagonal of the supercell is given. Color code shows values from -0.15 (blue) to 0.15 e/ \mathring{A}^3 (red).

Charge density difference and nonlocal correlation binding energy density are calculated for the R0 system and given in Figures S10 and S11. For visualization of the nonlocal binding energy density we have used the JuNoLo code¹⁶ to recalculate them from the charge densities obtained using VASP.

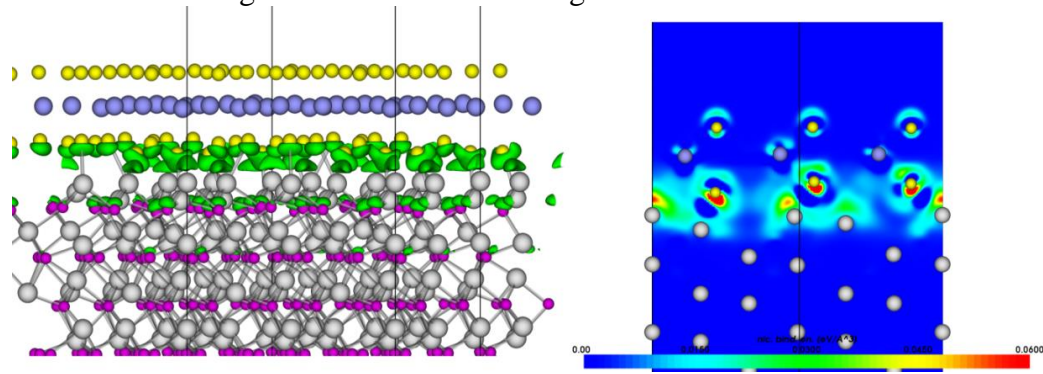


Figure S11. Nonlocal binding energy density - green isosurface (left) for the value 0.04 eV/Å^3 and inplane cross-section along the longer diagonal of the supercell (left) - values from 0 (blue) to 0.06 eV/Å^3 (red).

The nonlocal binding energy is 10% lower than the total binding energy, implying that all the other contributions are actually repulsive. We can therefore describe this adsorption as being almost exclusively van der Waals in nature (95% contribution), with some chemical modifications which are of repulsive character (5% contribution). Obviously, vdW interactions pull the MoS₂ layer closer to the Al₂O₃ surface gaining energy from nonlocal correlations, achieving optimum at such distances that even some repulsion can be allowed between the fragments. This type of adsorption is rather common and was named *physisorption with chemical modulation*¹⁷ for the case of graphene on Ir(111) or *weak adsorption and strong interaction*¹⁸ for graphene on Ni(111) surface.

However, this particular system shows an even richer adsorption interaction picture than graphene on (111) metal surfaces which we try to elucidate below.

In describing the adsorption mechanism in the case of MoS₂ on Al₂O₃ surface we start from the results in Table 1. By doing naive lattice matching that involves straining the MoS₂ layer, we obtain by far as the best adsorption configuration R30. However, when the strain of the MoS₂ is taken into account so that the adsorption

energy (rather than the binding energy) is calculated, we discover that such a configuration would not even be possible - i.e. in total it would not represent an energy gain and would be unstable. The origin of such large dependence of the binding energy on the MoS₂ strain lies in the source of the nonlocal binding energy (which is almost the complete value of the binding energy). Namely - looking at the nonlocal binding energy shape in Figure S11, we observe blobs formed around alumina and sulfur atoms. Nonlocal interaction energy stems from the interaction between electronic densities in these two regions which can be proven by reducing the nonlocal correlation interaction length, as for example in refs. 16 and 19 but it is beyond the scope of this paper. The important thing to notice is that the amount of this interaction is very sensitive to relative positions of sulfur and alumina atoms and applying a strain on the MoS₂ layer (even a small strain) can cause a very good registry of the S-Al atoms (very regular pattern in which many of the S-Al pairs are very close yielding large amounts of the vdW interaction) giving rise to an unphysically large binding energy. It is not impossible that layered structures such as MoS₂ attain some strain in order to keep a certain registry with the substrate yielding in total the largest adsorption energy. A very nice example is graphene on Ir(111) which grows in a 10×10 over 9×9 Moiré structure, where also a part of the strain in graphene is compensated by its buckling. Modeling such a situation in the MoS₂/Al₂O₃ system is however beyond the scope of this paper.

The main difference between MoS_2 on sapphire as compared to graphene on (111) metallic surfaces is the much smoother electronic structure of the metallic surfaces which makes the system much less sensitive to the exact relative position of the carbon atoms with respect to the underlying metal. With MoS_2 on sapphire, the row (point)-like structure of the Al_2O_3 surface shows large sensitivity to the relative positions of sulfur atoms with respect to the alumina atoms of the surface.

Theoretical calculations based on DFT could in principle determine the best orientation and relative position of the MoS₂ layer structure with more precision if enough CPU power were available to perform calculations for large cells with small strains.

We expect the MoS_2 structure in the experiment to have a very small strain growing in specific orientation with the surface obtaining the largest possible binding energy almost exclusively from the vdW interactions between sulfur-alumina atoms. From the energy differences obtained in our calculations, we conclude that one specific configuration will be dominant and stable at given temperatures, while still keeping relatively small energy barriers between different orientations yielding unlikely growth in the less favorable directions and remaining there due to slow kinetics. The influence of the edges in the finite triangle-shaped structures remains elusive at the moment – however, monolayer structure should determine stability in the thermodynamic limit.

Based on the DFT findings presented above, we decided to make the simplest possible model of van der Waals adsorption for this system. Namely, we simulate adsorption of the MoS_2 monolayer on the sapphire surface by simply calculating only the semi-empirical vdW contributions,²¹ based on pairwise atomic interactions:

$$E_{bind} = -\sum_{i,j} \frac{C_6}{r_{ij}^6} \tag{2}$$

We sum over all pairs of bottom sulfur atoms and top alumina atoms since all other contributions are much smaller because of the $1/r^6$ dependence of the vdW force, also indicated by the DFT calculations.

We use the C_6 value of 1 since it is a simple scaling factor and we are only interested in the difference between various configurations. However, for the given adsorption energies per MoS_2 unit in Figure S12 one can perform rescaling by taking the adsorption energy value as obtained from DFT calculations per MoS_2 unit cell as the average value.

This model, however simple - to our surprise, yields results short of spectacular. Namely, it predicts clearly a single orientation and position as the absolutely best one while all the other orientations of the MoS₂ layer relative to the surface - and all corresponding positions - are almost identical in energy. This means that the MoS₂ layer would rotate and slide without any energy penalty until it finds the best possible configuration for adsorption - dictated solely by vdW interactions. We believe that this result is general for all vdW heterostructures and hence we suggest this method as an excellent tool for prediction of such structures.

For calculations, we took an unstrained MoS_2 monolayer with a given relative rotation of the unit cell relative to the sapphire surface. MoS_2 was at an average height from the sapphire surface as obtained from the DFT calculations (3.24 Å from top Al to Mo). In addition, we also tested two other heights, one 0.2 Å above and other 0.2 Å below the selected value. The binding energy is calculated for 1600 relative positions of MoS_2 with respect to the surface. In each calculation at least 2000 sulfur atoms were involved. Results are given in Figure S12.

What is visible from the results in Figure S12 is that almost all orientations and relative positions of the MoS_2 monolayer with respect to the surface have identical binding energies which depend only on the distance between MoS_2 and the surface getting larger as MoS_2 approaches the surface. However, 0° and 60° orientations are very different from the rest, showing an enormous sensitivity to the exact arrangement of MoS_2 over the sapphire surface and a typical eggbox shape of the potential.

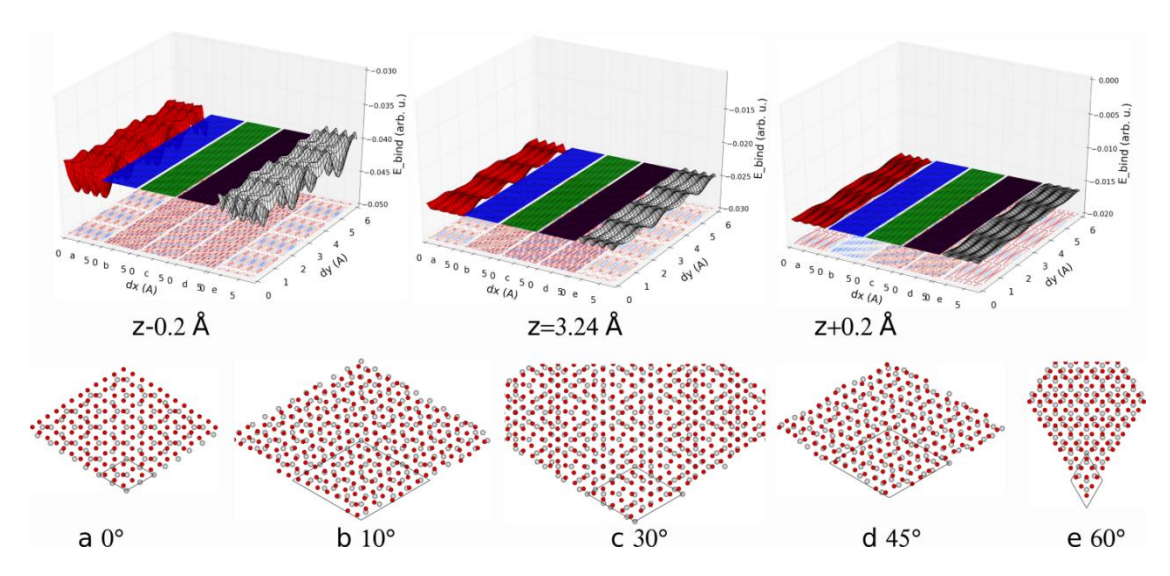


Figure S12. Top row, binding energies for three distances of MoS_2 with respect to the surface. In each plot 5 stripes are given corresponding to appropriate MoS_2 rotations with respect to the sapphire (shown in the second row - only top AI and bottom S atoms are drawn). a-red, b-blue, c-green, d-gray and e-white. Each point on a stripe corresponds to a relative x-y shift of the MoS_2 layer with respect to the sapphire surface (0,0 shown in bottom row). Bottom left corner of each stripe corresponds to dx,dy=(0,0) while top right point is (6 Å,6 Å). Below each stripe the contour plot is also given.

To determine the sensitivity of the eggbox potential on the orientation of the MoS_2 monolayer, we compare results for 0° and 2° rotation in Figure S13.

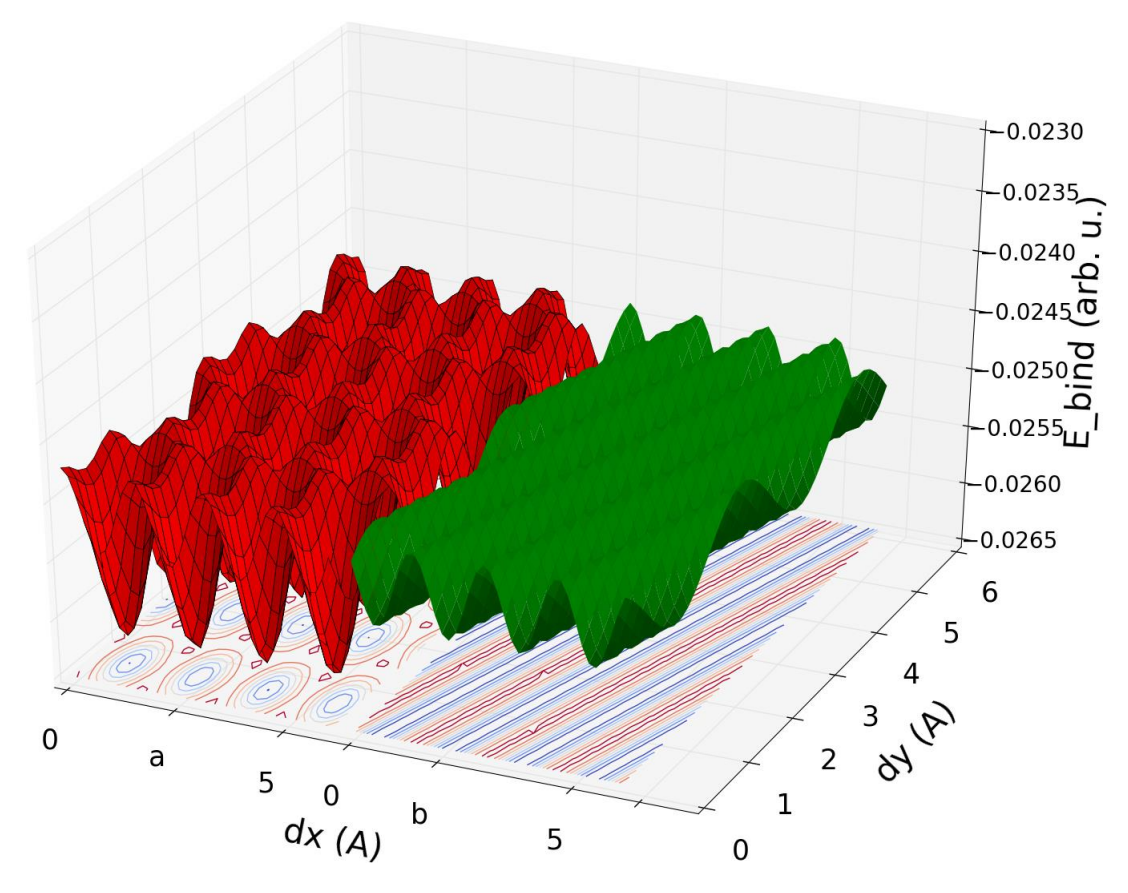


Figure S13. Binding energy as a function of MoS_2 rotation (0 degrees -red, 2 degrees -green) and on the relative x-y shift calculated in the 0-6 Å range in both x and y directions.

From Figure S13, it is obvious that the exact registry determined by the MoS_2 rotation with respect to the surface is crucial for the binding energy achieved through vdW interaction. To realize the special pattern that is characteristic of 0° rotation of the MoS_2 , we show two such structures in Figure S14 - one with zero x-y shift and the optimally positioned MoS_2 yielding one of the adsorption minima in Figure S13.

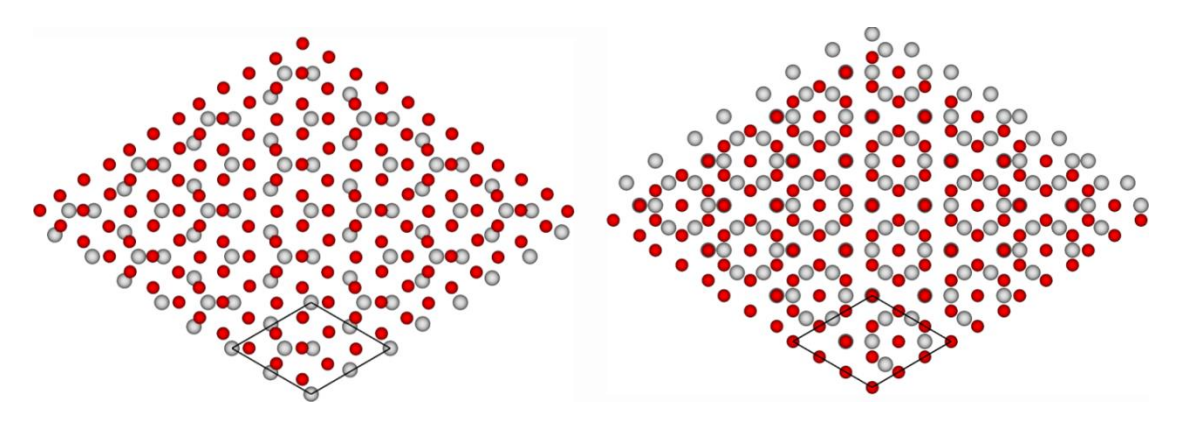


Figure S14. Rotation of 0 degrees with two different x-y shifts. Left - shift (0,0), right - optimal shift yielding the maximum adsorption energy.

Figure S14 reveals the simple mechanism behind preferential orientation and position for the vdW adsorption. Namely, at the optimal configuration almost all sulfur atoms have an identical small distance to either one or 2 top alumina atoms yielding a maximum amount of vdW energy. Such configuration is extremely sensitive to small movement of the MoS₂ structure unlike the other structures - shown in figure S13 (b,c,d) where every sulfur atom has different surroundings of alumina atoms. It is somewhat expected that such structure is less sensitive to exact positions of the MoS₂ layer since the x-y movement simply exchanges surroundings of the sulfur atoms - yielding again similar distribution of surroundings only attributed to different sulfur atoms. More surprising was that such different structures with various rotations of the MoS₂ layer will yield almost exactly the same amount of binding energy.

Finally, we would like to draw a parallel with Lego bricks - portrayed in a figure of the paper which strongly promotes the idea of the vdW heterostructures. Sapphire surface can be seen as a large Lego brick surface while the MoS₂ structure is another one smaller one. One can put MoS₂ onto the surface at any given position and orientation and the gravity (equivalent to vdW force in our model) will keep it bounded to the surface very weakly. One can try attaching it stronger to the surface but this would require exact arrangement both orientation with respect to the dips as well as the relative shift - so that it snaps in place yielding the strongest possible binding – Figure S15.

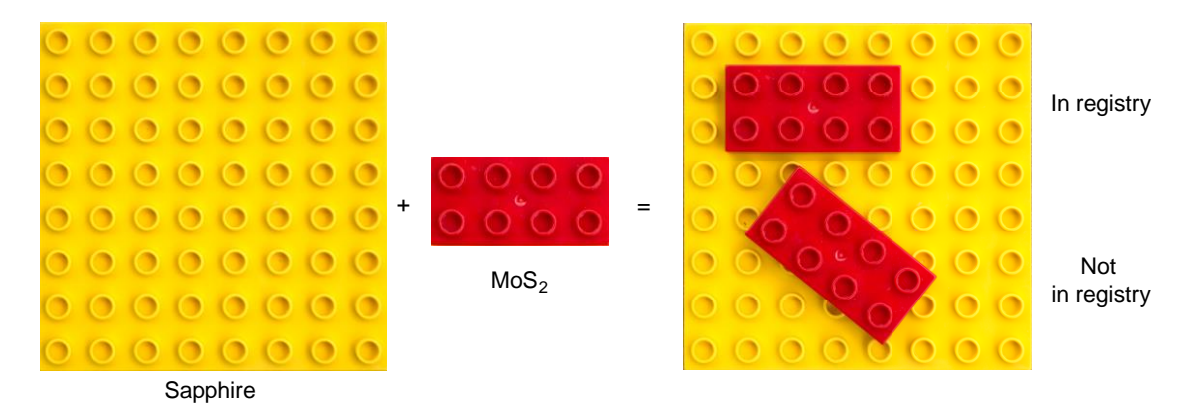


Figure S15. Analogy with Lego bricks. Only the correct orientation and lattice will give rise to an increased interaction between the surface and the overlayer.

5. Electrical transport measurements: single crystals

For electrical transport measurements on single crystals in four-probe geometry, we first transfer CVD-grown single domains of MoS₂ onto a degenerately doped Si substrate covered with 270 nm thick SiO₂ using PMMA A2 as a support film and etching in 30% KOH to detach the polymer film from the sapphire substrate. After transfer, the PMMA film is dissolved in acetone and residues are removed by annealing in Ar atmosphere at 350°C for 5 hours. PMMA A4 was used as the etching mask during oxygen plasma etching, (Figure S16a). We deposit 90 nm thick gold electrodes. The devices are then annealed at 200°C in Ar atmosphere to eliminate resist residues and reduce contact resistance.

In a second annealing step, the devices were annealed in vacuum (5×10^{-7} mbar) for ~15 hours at 130-140°C in order to remove water and other adsorbates from the surface of the 2D semiconducting channel.²³ Electrical measurements were performed immediately after this in vacuum. Figure S16b shows the current vs. bias voltage (I_{ds} vs. $V_{\rm ds}$) characteristics of our device for several different values of the gate voltage $V_{\rm g}$. The observed linear I_{ds} - V_{ds} characteristics indicate the high quality of contacts and the absence of significant charge injection barriers at room temperature. Figure S16c shows the transfer characteristics (I_{ds} vs V_g) of the device from Figure S16a recorded for a bias voltage $V_{ds} = 2$ V. The source-drain distance is L = 6.7 µm, $l_{12} = 4$ µm is the distance between the voltage probes V_1 and V_2 and the device width $W = 8.3 \mu m$. From this curve, we can obtain the field-effect mobility μ_{FE} defined as $\mu_{\rm FE} = [dG/dV_{\rm g}] \times [l_{12}/(WC_{\rm ox})]$ where G is the four-probe conductance defined as $G = I_{ds}/(V_1-V_2)$ with I_{ds} the drain current, $V_1 - V_2$ the measured voltage difference between the voltage probes and $C_{\text{ox}} = 1.3 \times 10^{-4} \text{ F/m}^2$ the capacitance between the channel and the back gate per unit area. At high gate voltages we observe the mobility reach a value of 43 cm²/Vs, comparable to results from previous two-terminal measurements on CVD MoS₂ (ref. 24) and slightly higher than in several reports on devices based on exfoliated MoS₂. ^{23, 25} Typical FETs produced using exactly the same fabrication procedure as the CVD material, with the absence of transfer and related possible polymer film contamination, show peak room-temperature mobilities in the $20-30 \text{ cm}^2/\text{Vs range}$.

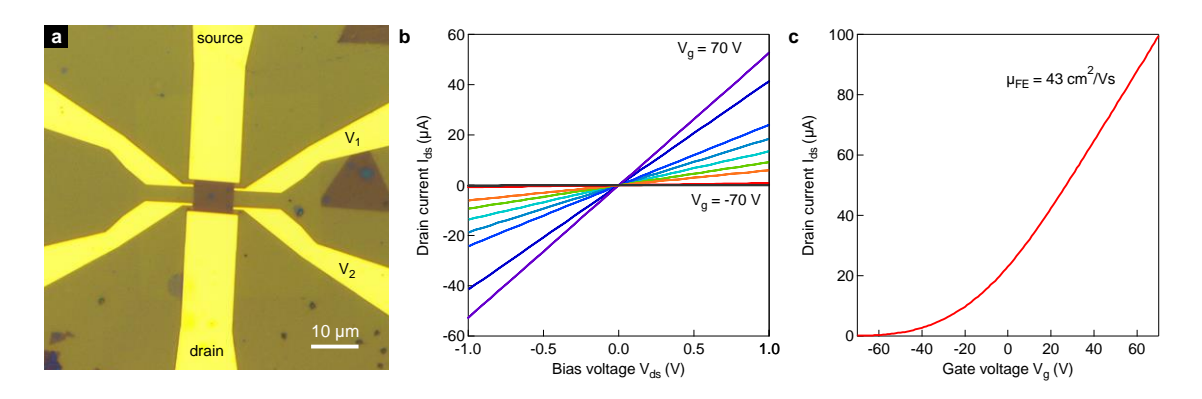


Figure S16. Electrical properties of single-crystal monolayer MoS₂. a, Optical image of a Hall-bar device based on a single-crystal island of MoS₂ transferred onto SiO₂. b, Sweeps of current I_{ds} vs. bias voltage V_{ds} characteristics of the device shown in a, indicating ohmic-like behavior of the contacts. c, Current as a function of gate voltage shows n-type behavior. We extract maximum field-effect mobility $\mu_{FE} = 43 \text{ cm}^2/\text{Vs}$.

6. Scanning Kelvin probe microscopy

In order to study the electrical properties of grain boundaries, new substrates were prepared with the aim of achieving significant doping levels by applying gate voltages in the ±10V range. This range of gate voltages is imposed by the AFM electronics. Metallic local gates consisting of Cr/Au (10/50 nm) were deposited on an intrinsic silicon substrate and covered with a 45 nm thick HfO₂ layer deposited by atomic layer deposition (ALD). CVD MoS₂ was then transferred from the sapphire growth substrate on the HfO₂ substrate with local gates, Figure S17a. Grain boundaries of each type formed by two single domains were then located using optical microscopy and 90 nm Au contacts were defined by electron beam lithography.

For the KPFM measurement a Cypher atomic force microscopy system (Asylum Research) was utilized allowing the simultaneous measurement of topography and local potential with spatial resolution of about 20 nm and a potential resolution of few millivolts. We used silicon KPFM probes (Olympus, OMCL-AC240TM) with a nominal tip radius of ~30 nm, which were covered with a conductive Ti/Pt (5/20 nm) layer and had a resonance frequency of ~70 kHz. An AC modulation voltage V_{AC} of 2 V was applied for the Kelvin probe measurements. An external bias between the two contacts (source and drain) $\hat{V}_{
m ds}$ of 1 V was applied and the gate voltage $V_{
m g}$ was varied between -6 and +6 V. The electrical current corresponding to $V_{\rm ds}$ was simultaneously recorded using an I/V converter. All measurements were performed under ambient conditions. The schematic drawing of the experimental setup and device geometry is shown on Figure S17a. On Figure S17b, we shown an example of a potential map acquired across two merging islands showing a relative orientation of 94°. Unlike in the cases presented in the main text, such a low-symmetry situation results in a twin grain boundary which manifests itself as an additional potential drop across the channel (Figure S17c), indicating that it introduces extra resistance, equivalent to an additional $\sim 4 \mu m$ long section of MoS₂.

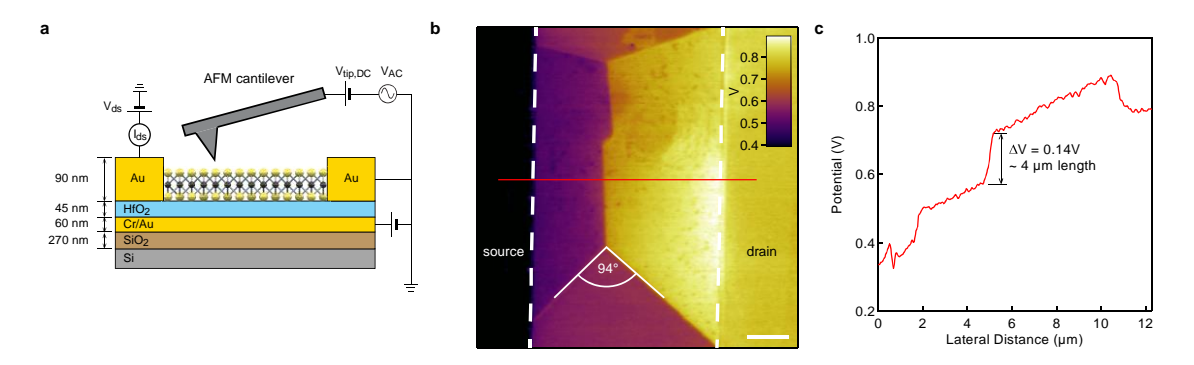


Figure S17. Scanning Kelvin probe imaging of grain boundaries. a, Schematic drawing of the setup and device layout for Kelvin probe imaging. b, Example of a potential map and potential profile across a resistive grain boundary formed between two single-crystal grains with a relative orientation angle that does not correspond to the high-symmetry direction of the MoS_2 lattice. Scale bar is 2 μ m long. c, Potential profile along the red line in b. The presence of a tilt grain boundary introduces additional voltage drop and resistance, equivalent to an additional section of MoS_2 with a length of 4μ m.

7. Electrical transport measurements: large-area films

Just like in the case of FETs based on single-crystal CVD MoS₂, the fabrication of large-area devices begins with the transfer procedure which has been optimized for transferring large-area films. Sapphire chips were first spin coated with PMMA 950 MW 2% in anisole at 1500 rpm for 60s and left in vacuum in a desiccator for 12 hours in order to remove the solvent from the resist. The resist was not baked in order to avoid possible build-up of mechanical stress. Films were detached in KOH (30%) at moderate temperatures (60-70 °C), washed in DI water and transferred on Si/SiO₂ chips, drying at 40 °C for 40 minutes. The resist was removed by dipping the sample in acetone for 12 hours, followed by rinsing with isopropanol and drying in N₂, followed by annealing in low vacuum (10⁻² mbar) for 5h at 350 °C in the flow of argon gas. This resulted in clean and intact films with large regions applicable for device fabrication and minimal damage caused by transfer process.

Prior to measurements, the devices are annealed in vacuum (5×10^{-7} mbar) for ~50 hours at 130-140°C in order to remove water and other adsorbates from the surface of the 2D semiconducting channel²³. The transfer characteristics (I_{ds} vs V_g) of the device recorded for a bias voltage $V_{ds} = 1$ V is shown on Figure S18a for different combinations of leads, as labeled in the inset of Figure 6 in the main manuscript. We can use two distinct configurations of leads: nearest neighbors, in which two neighboring leads are used as source and drain electrodes and other combinations allowing us to probe the full length of the device (\sim 80 µm) where the region between the source electrodes can contain multiple leads that are disconnected during the measurements. Such leads could be considered to represent invasive contacts and introduce additional scattering because of a local change in the chemical potential induced by the presence of a metal with a different work function than that of the semiconducting channel. This implies that mobilities obtained using such lead combinations could in fact be underestimated.

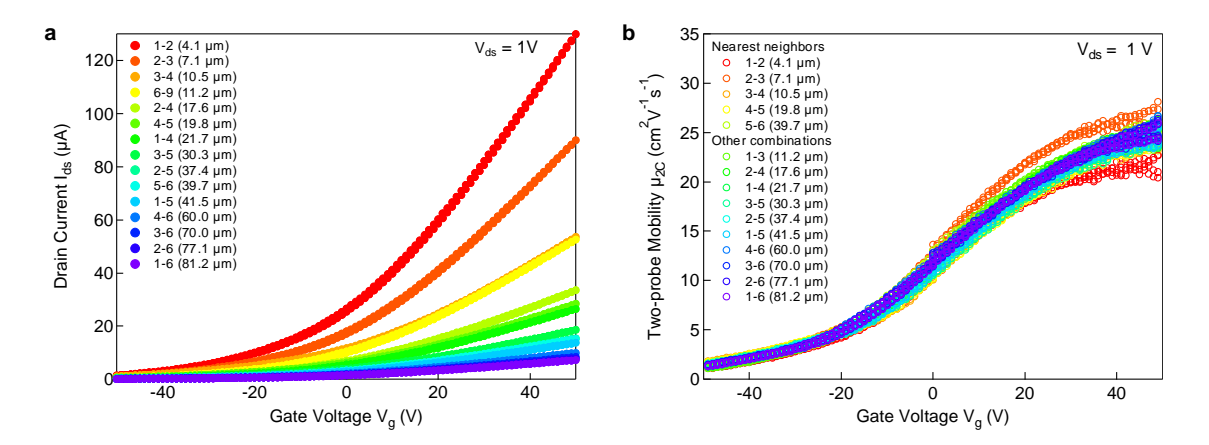


Figure S18. Electrical properties of large-area monolayer MoS₂. a, Drain current $I_{\rm ds}$ as a function of gate voltage recorded for different combinations of electrodes shown in the main Figure 6. b, Two-contact field-effect mobility extracted from the transconductance $g_{\rm m} = dI_{\rm ds}/dV_{\rm g}$ obtained by differentiating the curves in a.

By differentiating the transfer curves with respect to the gate voltage, we obtain the two-contact effective field-effect mobility μ_{2C} defined as $\mu_{2C} = [dI/dV_g] \times [L/(W\cdot C_{ox}\cdot V_{ds})]$ where I_{ds} is the drain current, L the channel length, W its width, V_{ds} the bias voltage and $C_{ox} = 1.3 \times 10^{-4} \text{ F/m}^2$ the capacitance between the channel and the back gate per unit area. Because the contact resistance is neglected (equivalent to assuming that the bias voltage V_{ds} corresponds to the entire voltage drop over the semiconducting channel), the obtained mobility values are underestimated. The obtained mobility values as a function of gate voltage are shown on Figure S18b and fall within the 20-27 cm²/Vs range at $V_g = 45\text{V}$ irrespective of the channel length or the combination of leads used (nearest neighbors or other).

The devices fabricated on continuous films are expected to contain numerous grains and were located without knowledge of the relative orientation of grains within the channel. We estimate the average triangle size for the CVD material based on which we fabricated the devices to be approximately 10 μm . We then estimate the lower bound for the defect density in the channel of our large-area transistors.

We consider the simplest case, where the triangles of the same size are regularly spaced and form 60° grain boundaries. This is schematically depicted on Figure S19 where triangles merge and form a continuous film, a segment of which is presented in the form of a big triangle, containing several grains. First, we position our transistor channel parallel to the long edge of triangles (blue transparent rectangle on Figure S19). Each triangle forms two grain boundaries with the neighbors along the current path. Based on a typical triangle edge length of 10 µm, we reach a lower estimate of a possible linear defect density to be 0.2 µm⁻¹. We notice that tilting the channel to the triangle edge will provide more grain boundaries. For example, a 90° tilt will result in an increased number of boundaries per unit length (green rectangle in Figure S19). More complicated cases, where the distance between the growth centers is smaller than that considered in our simple model and where 90° boundaries are taken into account, provide the increase of linear grain boundary density. We also notice that in reality, grain positioning will be much more complex. Based on this, we expect for a total length of 82 µm (device in the inset of Figure 6 in the main manuscript) at least 16 grain boundaries along the current path.

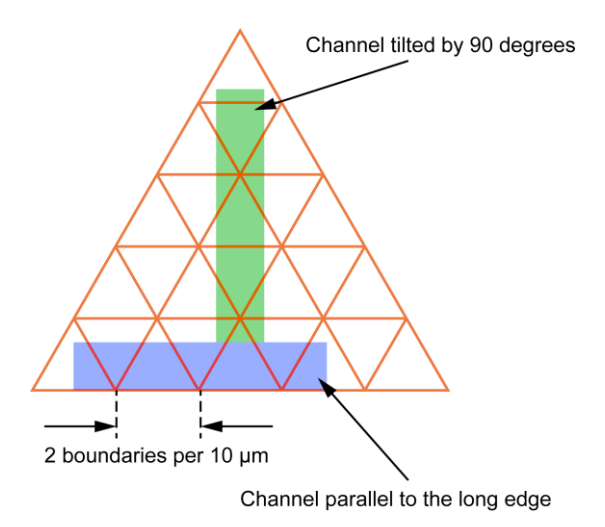


Figure S19. Schematic of channel location inside the continuous film. Schematic of the orientation of the transistor channel with respect to grains inside the continuous film.

References

- Brivio, J.; Alexander, D. T. L.; Kis, A. Ripples and Layers in Ultrathin MoS₂ Membranes. Nano Lett. 2011, 11, 5148-5153.
- 2. van der Zande, A. M.; Huang, P. Y.; Chenet, D. a.; Berkelbach, T. C.; You, Y.; Lee, G.-H.; Heinz, T. F.; Reichman, D. R.; Muller, D. A.; Hone, J. C. Grains and Grain Boundaries in Highly Crystalline Monolayer Molybdenum Disulphide. Nat. Mater. 2013, 12, 554-561.
- 3. Wood, E. A. Vocabulary of Surface Crystallography. J. Appl. Phys. 1964, 35, 1306-1312.
- 4. Paolo, G.; Stefano, B.; Nicola, B.; Matteo, C.; Roberto, C.; Carlo, C.; Davide, C.; Guido, L. C.; Matteo, C.; Ismaila, D., *et al.* Quantum Espresso: A Modular and Open-Source Software Project for Quantum Simulations of Materials. J. Phys.: Condens. Matter 2009, 21, 395502.
- 5. Sabatini, R.; Gorni, T.; de Gironcoli, S. Nonlocal Van Der Waals Density Functional Made Simple and Efficient. Physical Review B 2013, 87, 041108.
- 6. Vydrov, O. A.; Van Voorhis, T. Nonlocal Van Der Waals Density Functional: The Simpler the Better. The Journal of Chemical Physics 2010, 133, 244103
- 7. Blöchl, P. E. Projector Augmented-Wave Method. Physical Review B 1994, 50, 17953-17979.
- 8. Kresse, G.; Joubert, D. From Ultrasoft Pseudopotentials to the Projector Augmented-Wave Method. Physical Review B 1999, 59, 1758-1775.
- 9. Kresse, G.; Furthmüller, J. Efficient Iterative Schemes for *Ab Initio* Total-Energy Calculations Using a Plane-Wave Basis Set. Physical Review B 1996, 54, 11169-11186.
- 10. Kresse, G.; Hafner, J. *Ab Initio* Molecular Dynamics for Liquid Metals. Physical Review B 1993, 47, 558-561.
- 11. Dion, M.; Rydberg, H.; Schröder, E.; Langreth, D. C.; Lundqvist, B. I. Van Der Waals Density Functional for General Geometries. Phys. Rev. Lett. 2004, 92, 246401.
- 12. Klimeš, J.; Bowler, D. R.; Michaelides, A. Chemical Accuracy for the Van Der Waals Density Functional. J. Phys.: Condens. Matter 2010, 22, 022201.
- 13. Klimeš, J.; Bowler, D. R.; Michaelides, A. Van Der Waals Density Functionals Applied to Solids. Physical Review B 2011, 83, 195131.
- 14. Caciuc, V.; Atodiresei, N.; Callsen, M.; Lazić, P.; Blügel, S. *Ab Initio* and Semi-Empirical Van Der Waals Study of Graphene–Boron Nitride Interaction from a Molecular Point of View. J. Phys.: Condens. Matter 2012, 24, 424214.
- 15. Hyldgaard, P.; Berland, K.; Schröder, E. Interpretation of Van Der Waal Density Functionals. ArXiv 2014, 1408.2075.
- 16. Lazić, P.; Atodiresei, N.; Alaei, M.; Caciuc, V.; Blügel, S.; Brako, R. Junolo Jülich Nonlocal Code for Parallel Post-Processing Evaluation of Vdw-Df Correlation Energy. Comput. Phys. Commun. 2010, 181, 371-379.
- 17. Busse, C.; Lazić, P.; Djemour, R.; Coraux, J.; Gerber, T.; Atodiresei, N.; Caciuc, V.; Brako, R.; N'Diaye, A. T.; Blügel, S., *et al.* Graphene on Ir(111): Physisorption with Chemical Modulation. Phys. Rev. Lett. 2011, 107, 036101.

- 18. Mittendorfer, F.; Garhofer, A.; Redinger, J.; Klimeš, J.; Harl, J.; Kresse, G. Graphene on Ni(111): Strong Interaction and Weak Adsorption. Physical Review B 2011, 84, 201401.
- 19. Berland, K.; Hyldgaard, P. Analysis of Van Der Waals Density Functional Components: Binding and Corrugation of Benzene and C60 on Boron Nitride and Graphene. Physical Review B 2013, 87, 205421.
- Runte, S.; Lazić, P.; Vo-Van, C.; Coraux, J.; Zegenhagen, J.; Busse, C. Graphene Buckles under Stress: An X-Ray Standing Wave and Scanning Tunneling Microscopy Study. Physical Review B 2014, 89, 155427.
- 21. Grimme, S. Semiempirical Gga-Type Density Functional Constructed with a Long-Range Dispersion Correction. J. Comput. Chem. 2006, 27, 1787-1799.
- 22. Geim, A. K.; Grigorieva, I. V. Van Der Waals Heterostructures. Nature 2013, 499, 419-425.
- 23. Baugher, B.; Churchill, H. O. H.; Yang, Y.; Jarillo-Herrero, P. Intrinsic Electronic Transport Properties of High Quality Monolayer and Bilayer MoS₂. Nano Lett. 2013, 13, 4212-4216.
- 24. Schmidt, H.; Wang, S.; Chu, L.; Toh, M.; Kumar, R.; Zhao, W.; Castro Neto, A. H.; Martin, J.; Adam, S.; Özyilmaz, B., *et al.* Transport Properties of Monolayer MoS₂ Grown by Chemical Vapor Deposition. Nano Lett. 2014, 14, 1909-1913.
- 25. Radisavljevic, B.; Kis, A. Mobility Engineering and a Metal-Insulator Transition in Monolayer MoS₂. Nat. Mater. 2013, 12, 815-820.
- 26. Najmaei, S.; Amani, M.; Chin, M. L.; Liu, Z.; Birdwell, A. G.; O'Regan, T. P.; Ajayan, P. M.; Dubey, M.; Lou, J. Electrical Transport Properties of Polycrystalline Monolayer Molybdenum Disulfide. ACS Nano 2014, 8, 7930-7937.